ACS OMEGA

http://pubs.acs.org/journal/acsodf

Article

Nanocomposites with ZrO_2@S-Doped g-C_3N_4 as an Enhanced Binder-Free Sensor: Synthesis and Characterization

Nigussie Alebachew,* H. C. Ananda Murthy,* Bedasa Abdisa Gonfa,* Karel G. von Eschwege, Ernst H. G. Langner, Elizabeth Coetsee, and Taye B. Demissie*

Cite This: *ACS Omega* 2023, 8, 13775−13790

Read Online

ACCESS | Metrics & More | Article Recommendations | Supporting Information

ABSTRACT: This study describes new electrocatalyst materials that can detect and reduce environmental pollutants. The synthesis and characterization of semiconductor nanocomposites (NCs) made from active ZrO_2@S-doped g-C_3N_4 is presented. Electrochemical impedance spectroscopy (EIS) and Mott-Schottky (M-S) measurements were used to examine electron transfer characteristics of the synthesized samples. Using X-ray diffraction (XRD) and high-resolution scanning electron microscopy (HR-SEM) techniques, inclusion of monoclinic ZrO_2 on flower-shaped S-doped-g-C_3N_4 was visualized. High-resolution X-ray photoelectron spectroscopy (XPS) revealed successful doping of ZrO_2 into the lattice of S-doped g-C_3N_4. The electron transport mechanism between the electrolyte and the fluorine tin-oxide electrode (FTOE) was enhanced by the synergistic interaction between ZrO_2 and S-doped g-C_3N_4 as co-modifiers. Development of a platform with improved conductivity based on an FTOE modified with ZrO_2@S-doped g-C_3N_4 NCs resulted in an ideal platform for the detection of 4-nitrophenol (4-NP) in water. The electrocatalytic activity of the modified electrode was evaluated through determination of 4-NP by cyclic voltammetry (CV) and differential pulse voltammetry (DPV) under optimum conditions (pH 5). ZrO_2@S-doped g-C_3N_4 (20%)/FTOE exhibited good electrocatalytic activity with a linear range from 10 to 100 μM and a low limit of detection (LOD) of 6.65 μM. Typical p-type semiconductor ZrO_2@S-doped g-C_3N_4 NCs significantly impact the superior detection of 4-NP due to its size, shape, optical properties, specific surface area and effective separation of electron−hole pairs. We conclude that the superior electrochemical sensor behavior of the ZrO_2@S-doped g-C_3N_4 (20%)/FTOE surfaces results from the synergistic interaction between S-doped g-C_3N_4 and ZrO_2 surfaces that produce an active NC interface.

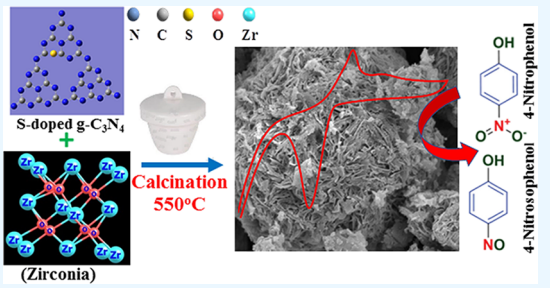

1. INTRODUCTION

The world has been facing huge environmental degradation issues in recent years due to rapid industrialization. Researchers are developing several new instrumental techniques and strategies to maintain a secure environment; however, efficiency and costs are often not yet optimized. Recently, different methods have been developed to detect 4-NP by the use of semiconductor nano-composites.[1−3] In this aspect, nitro-phenols have the potential to cause significant harm to humans, plants, microbes, and plankton. Nowadays, due to their expanding use in the production of drugs, fungicides, herbicides, insecticides, and dyes, nitro-phenols have become focus areas of research.[4−9]

Utilization of a few semiconductor-based materials from carbon-rich resources effectively and efficiently is generally regarded as one of the many potential options. Many researchers have employed graphitic carbon nitride (g-C_3N_4) for electrochemical sensing of dangerous environmental pollutants because of its ideal band gap value of 2.7 eV.[10,11] Therefore, since its introduction, g-C_3N_4 has drawn significant attention due to its exceptional characteristics and unusual atomic and electronic structures. However, few intrinsic characteristics, such as its small specific surface area and rapid recombination of photogenerated electron−hole pairs, limit its usage. Computational[12,13] and band gap studies[14] were employed to find ways to improve these properties. Researchers often focused on altering surfaces by a variety of methods, such as calcination at various temperatures,[15] doping with nonmetals,[16,17] and studying the effects of metal and metal oxides[18] on different precursors.[19] More details of the local structure, optical characteristics, and composition of the fabricated g-C_3N_4-based NC materials are not properly discussed in many publications and thus uncertainty prevails in many aspects.[20−22]

Unfortunately, g-C_3N_4 has a strong visible-light response due to its easily produced electrons and holes under visible-light irradiation. Its photogenerated electron−hole pairs are

Received: December 25, 2022
Accepted: March 22, 2023
Published: April 3, 2023

Scheme 1. Schematic Illustration of the Preparation of ZrO_2@S-Doped g-C_3N_4 NCs and Their Application for Detecting Hazardous 4-Nitrophenol

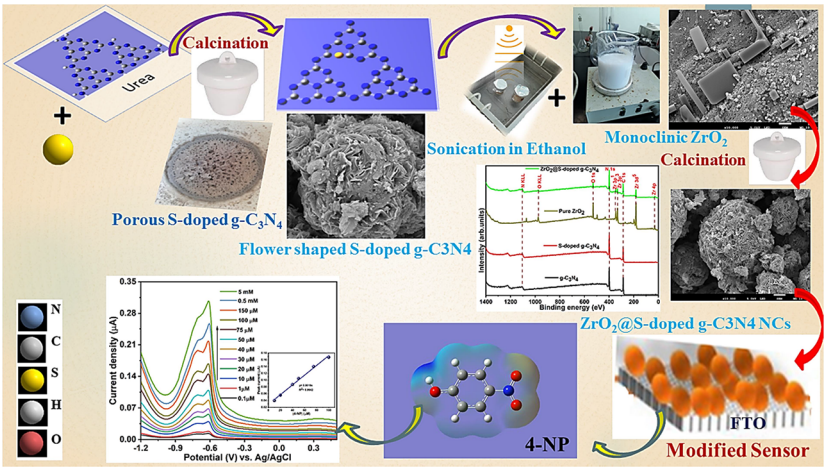

easy to recombine.[23] Recent research has shown that there is still opportunity for advancement in the geometric and electrical properties of composites based on g-C_3N_4. Doping g-C_3N_4 with metal oxide and nonmetal elements may greatly enhance its electrical and optical properties. Recently, g-C_3N_4-based NCs were synthesized by doping with metal oxides such as TiO_2[24] and the nonmetal element like S with high visible light photocatalytic activity or by pyrolysis of C and N-rich materials like urea and thiourea.[17,25−27] This was done to develop sensors,[21] supercapacitors,[28] and photocatalytic surfaces.[29] However, there are many unclarified aspects since the finer details of these new materials' local structure, optical properties, and composition are not clearly described in many reports dealing with this topic.

g-C_3N_4 has exceptional properties such as high mechanical strength, good chemical stability, high level of oxygen-ion conductivity, wide band gap value, corrosion resistance, and low thermal conductivity.[30−32] It has applications such as electro-optical materials, good thermal stabilities, and fuel-cell technology sensors.[20,33] Zirconium oxide (zirconia, ZrO_2) was utilized to enhance the catalytic properties of semiconductors such as g-C_3N_4. It is also used as a co-catalyst or co-photocatalyst in g-C_3N_4 heterojunction systems to improve some of the drawbacks of pure g-C_3N_4, such as rapid recombination of photogenerated electron−hole pairs and insufficient visible light absorption.

Zirconia studies reveal cubic, tetragonal, or monoclinic structures (space group C2/c) characterized by strong electron correlation and a larger band gap than 3 eV.[32] Even though there are reports about the use of ZrO_2 NPs to improve the optical and electrical properties of g-C_3N_4 for photocatalytic degradation of rhodamine B (RhB),[33] photocatalytic degradation of methylene blue,[20] and photocatalytic activity for degradation of 4-chlorophenol,[34] discussions of geometrical and electrical structures and electrolytic sensor activity of the ZrO_2@g-C_3N_4 heterojunction are still unclear and missing from the literature. It is also important to mention that the benefits of fabricated electrodes include ease of construction, wide surface area, improved conductivity, chemical stability, non-toxicity, and electrochemical activity. Therefore, in this study, we evaluate the synthesis, characterization, functionality, and sensor application of ZrO_2@S-doped g-C_3N_4 electrodes for the first time without using binders or carbon materials to create modified electrodes for 4-NP sensing. Through the current work, we also established the groundwork for upcoming syntheses, clarifications, and a prospective use of such semiconducting NCs. Scheme 1 presents an overall schematic representation for their preparation and application processes.

2. MATERIALS AND METHODS

2.1. Materials. All the reagents and chemicals were of analytical grade and used without further purification. These include urea ($CO(NH_2)_2$), ammonium sulfate ($(NH_4)_2SO_4$), absolute ethanol (C_2H_5OH, 97%), sulfuric acid (H_2SO_4), sodium hydroxide (NaOH), ammonium hydroxide (NH_4OH), zirconia oxychloride hydrated ($ZrOCl_2{\cdot}8H_2O$), potassium ferric-hexa-cyanide ($K_3Fe(CN)_6$), dimethyl formamide (DMF), dimethyl sulfoxide (DMSO), potassium chloride (KCl), and hydrochloric acid (HCl, 98%). 4-nitrophenol ($C_6H_5NO_3$) and alumina (Al_2O_3) were obtained from Sigma-Aldrich and monosodium hydrogen phosphate (NaH_2PO_4) and disodium hydrogen phosphate (Na_2HPO_4) from Samir Tech-Chem, India. 4-NP was selected as the target contaminant and used as supplied. A potentiostat (Autolab Ivium Technologies B V De Zaale 11 5612 AJ Eindhoven, Netherlands) coupled with a personal computer was used for electrochemical studies.[3]

2.2. Preparation of Sulfur-Doped Graphitic Carbon Nitride (S-Doped g-C_3N_4). The S-doped g-C_3N_4 NC was prepared by modifying an upgraded gas templating method.[35] Briefly, ammonium sulfate ($(NH_4)_2SO_4$, 2 g) and a fixed amount of urea ($CO(NH_2)_2$, 8 g) were used via the following process. First, $(NH_4)_2SO_4$ was placed at the bottom of a crucible, distributed uniformly, and then, urea was uniformly laid over ammonium sulfate. The crucible was covered with alumina foil and placed into a muffle furnace at 550 °C with a temperature ramp rate of 15 °C min^{-1} for 4 h. After cooling the furnace, the prepared bulk material was dissolved in 100 mL of ethanol and sonicated for 2 h. The resulting sulfur-doped graphitic carbon nitride sample was centrifuged at 4000 rpm to eliminate the unexfoliated impurities. The material was filtered and then dried at room temperature. Bulk g-C_3N_4 was prepared by pyrolysis of urea under similar reaction conditions and in the absence of sulfur.[3] This was done by pyrolyzing urea at the same heating temperature and heating time.

https://doi.org/10.1021/acsomega.2c08174
ACS Omega 2023, 8, 13775−13790

2.3. Synthesis of ZrO_2@S-Doped g-C_3N_4 NCs. ZrO_2@S-doped g-C_3N_4 NCs were prepared from ZrO_2 powder and the S-doped g-C_3N_4 NCs following a previously reported method.[33] First, approximately, 6.5 g of $ZrOCl_2{\cdot}8H_2O$ was added to 100 mL of deionized water to prepare 0.2 mol L^{-1} $ZrOCl_2$ aqueous solution. Ammonia water was slowly added to adjust the pH to 10−11 and stirred until a white zirconia (ZrO_2) precipitate was formed. On the other hand, a homogenous solution of zirconia was added to the measured S-doped g-C_3N_4 and stirred for 4 h. After filtering and repeated washing with distilled water and ethanol, the sample was left in an oven at 60 °C overnight and then in a muffle furnace at 500 °C for 3 h, at a heating rate of 15 °C min^{-1}. After cooling, ZrO_2@ S-doped g-C_3N_4 heterostructure, ZrO_2@S-doped g-C_3N_4 (5%), ZrO_2@S-doped g-C_3N_4 (10%), ZrO_2@S-doped g-C_3N_4 (20%), and ZrO_2@S-doped g-C_3N_4 (30%) NCs were prepared. For comparison, pure ZrO_2 NPs were synthesized from the precursor $ZrOCl_2{\cdot}8H_2O$ by chemical combustion precipitation. The growth of ZrO_2@S-doped g-C_3N_4 was controlled by applying the same synthesis method and conditions such as constant reactant concentration, stirring, pH, temperature, time, and the same chemical environment.[36]

2.4. Material Characterization. As per our earlier report,[3] the phase structure of the samples was studied by powder X-ray diffraction (XRD) with X-ray tube Cu Kα radiation target Cu, a voltage of 40.0 kV, and current of 30.0 mA at a scanning rate of 3.0 deg/min (SHIMADZU Corporation, Japan, Model XRD-7000X-RAY diffractometer). The phase purity was evaluated using Fourier transform infrared (FTIR) spectroscopy measured on Spectrum 65 FT-IR (PerkinElmer) in the range 4000−400 cm^{-1} (resolution: 4 cm^{-1}, number of scans: 4) in KBr pellets. Optical properties were investigated by ultraviolet−visible (UV−vis) diffused reflectance spectra (DRS) using a scanning-type UV−vis spectrometer (Perkin Elmer, Lambda 950) with a $BaSO_4$-based integrating sphere in the wavelength range of 200−800 nm. Capillary tubes and a digital melting point device were used to assess the thermal stability and degradation of the samples. Thermogravimetric analysis (TGA) and differential thermal analysis (DTA) were performed under an N_2 atmosphere (20 mL/min) using a DTG-60H Shimadzu thermal analyzer. TGA/DTA techniques were performed with a NETZSCH STA 409 PC/ PG, at a heating rate of 15 °C min^{-1} applied between room temperature and 1000 °C. Using a xenon (Xe) flash lamp as the excitation source, steady photoluminescence (PL) spectra were recorded on a Cary Eclipse fluorescence spectrophotometer (Agilent, Malaysia).[3]

Morphological features of the prepared samples were visually characterized by using high-resolution scanning electron microscopy/energy-dispersive X-ray spectroscopy/secondary electron diffraction (HR-SEM/EDS/SAED) HR-SEM: JEOL 7800F Field Emission SEM, with an Oxford EDS and EM: JEOL IT200 SEM, with a JEOL EDS. X-ray photoelectron spectroscopic (XPS) analysis (model PHI 5000 Versaprobe) was conducted to study the chemical compositions of the prepared heterostructured materials. To reduce charging on the surface, a low-energy Ar^+ ion gun and low-energy neutralizer electron gun were employed. A 100 μm diameter monochromatic Al Kα X-ray beam ($h\nu$ = 1486.6 eV) generated by a 25 W; 15 kV electron beam was used to investigate different binding energy peaks. Multipack version 9.8 software was used to examine the spectra to distinguish the chemical compounds and their electronic states by means of Gaussian−Lorentz fits. Nitrogen adsorption−desorption isotherms and the Brunauer−Emmett−Teller method were applied for the surface area and porosity measurements (isotherms), which were obtained with an ASAP 2020 surface area and porosity analyzer from Micrometrics with ASAP 2020 v2.0 software installed.[3] Data refinement was done using Microactive v1.01 software. Approximately, 30 mg of samples was activated under vacuum at 150 °C for 16 h. All the samples were cooled to room temperature, and N_2 adsorption−desorption measurements were done at 77 K.

2.5. Preparation of 4-Nitrophenol Solution. 0.5 mM stock solution of 4-NP was prepared by dissolving 70 mg of 4-NP in 100 mL of distilled water and then making up to 1000 mL in a volumetric flask. Using the proper dilution with 0.1 M phosphate buffer solution (PBS, pH = 7.0), a series of 4-NP working solutions were prepared from the stock solution. All solutions were prepared using deionized water, and all measurements were done at room temperature.[3]

2.6. Preparing Binder-Free Electrodes. Before modification, the bare fluorine tin-oxide electrode (FTOE) was polished using 0.05 mm Al_2O_3 polishing powder, followed by thorough washing with ultrapure water and successive ultrasonication with acetone, absolute ethanol, and deionized water, respectively, for 15 min each time. This procedure was done repeatedly throughout this study to ensure that there was no contamination. After drying, the electrode was sealed with Scotch tape with an exposed geometric area of 1 cm^2. To disperse the synthesized NCs, 0.5% wt solution of NCs was prepared in DMF solvent by sonicating vigorously for 2 h at room temperature. The resulting suspension (25 μL) was utilized for drop cast deposition on FTOE, where the modified electrodes were obtained after drying. Afterward, the dried modified electrodes were gently washed with deionized water to remove loosely attached samples on the modified electrodes' surface. Finally, the modified binder-free electrodes were used for electrochemical measurements. 4-NP, a known environmental pollutant,[2,37] was used to demonstrate the sensing ability of the modified electrode.

2.7. Electrochemical Experiments. Cyclic voltammetry (CV) and differential pulse voltammetry (DPV) experiments were performed by three conventional electrodes in an electrochemical cell with Ag/AgCl (3.0 M KCl aqua electrolyte) as the reference electrode, platinum wire as the counter electrode, and fluorine tin-oxide electrode (FTOE) (1 × 1 cm^2) coated with ZrO_2@S-doped g-C_3N_4, S-doped C_3N_4, g-C_3N_4, and ZrO_2 as working electrodes, connected to a potentiostat coupled to a personal computer. The phosphate buffer solution (PBS, 0.1 M) electrolyte was prepared using anhydrous sodium phosphate (Na_2HPO_4) and monobasic anhydrous salts (NaH_2PO_4) with pH variation from 4 to 11 through application of 0.1 M HCl and 0.1 M NaOH and using a pH meter. CV and DPV assays were performed in the potential range of −1.2 to 0.6 V with a 50 mV s^{-1} scan rate.

Electrochemical impedance spectroscopy (EIS) measurements were performed by using 5 mM $Fe(CN)_6^{-3}/Fe(CN)_6^{-4}$, applying an AC potential with an amplitude of 5 mV in the frequency range from 0.1 to 1 × 10^{-5} Hz and an applied potential of 0.22 V. A Mott-Schottky curve study was obtained by using a two-electrode configuration test in 0.5 M Na_2SO_4 solution to evaluate the electrochemical performance of the electrodes.

2.8. Computational Methods. We used our previously constructed *s*-triazine rings to study some features of the

https://doi.org/10.1021/acsomega.2c08174
ACS Omega 2023, 8, 13775−13790

materials.[3] Similar to our previous study, the findings of the geometric optimizations of pure g-C_3N_4, S-doped g-C_3N_4, and ZrO_2 models were used as inputs in the *Gaussian* 09 program package.[38] The electrical properties of optimized geometries, wavefunctions, and energies of all the structures were estimated via DFT simulations using the Becke-3-Lee-Yang-Parr (B3LYP) hybrid functional[39−41] and the 6-31 + G(d,p) basis set. Results were visualized using Chemcraft 1.8 and Gaussview software.

3. RESULTS AND DISCUSSION

To better understand the key reaction parameters when converting ammonium sulfate and urea on the S-doped g-C_3N_4 sheets, we explored the retainability and delayed release impacts of pyrolysis-generated self-supporting atmosphere and reaction temperature. The surface of a closed crucible was found to produce a pale-yellow ornamented solid when a specific amount of ammonium sulfate was added. However, in an open crucible, every component was thermally annihilated, and no solids formed on the crucible's surface. According to earlier studies, placing gas sources like ammonium sulfate below urea resulted in the drifting of gases from the bottom to the top of the crucible, utilization of decomposed gases, and disruption of bulk g-C_3N_4.[35]

3.1. XRD Study. To verify the crystal structures of pristine g-C_3N_4, S-doped g-C_3N_4, ZrO_2@S-doped g-C_3N_4 (5, 10, 20, and 30%) NCs, and ZrO_2 NPs, XRD studies were conducted. Figure 1 shows the two significant peaks observed for bulk g-C_3N_4 and S-doped g-C_3N_4. The low-intensity peak at 2θ = 13.4° and a strong peak at 27.99° are attributed to (100) and (002) diffraction planes, respectively, indicating the unique graphitic structure of pure g-C_3N_4.[42] Compared to bulk g-C_3N_4, the strong peak in S-doped g-C_3N_4 is sharper and more intense, indicating a more crystalline nature than g-C_3N_4.

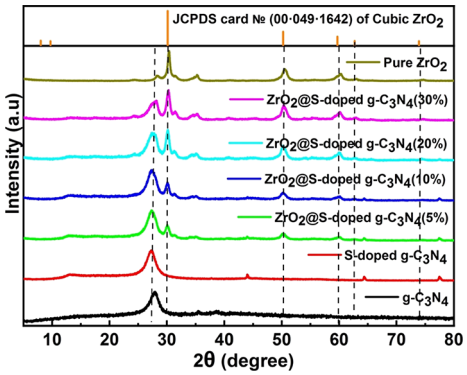

Figure 1. XRD pattern of bulk g-C_3N_4, S doped g-C_3N_4, and ZrO_2@S-doped g-C_3N_4 (5, 10, 20, and 30%,) NCs and pure ZrO_2.

The main peak of S-doped g-C_3N_4 was found to be shifted negatively to 2θ = 26.99°, indicating the presence of impurities, in this case, S atoms in the precursor material substituted for N atoms. Pure ZrO_2 has a cubic phase with the corresponding characteristic peaks at 2θ = 30.22,35.27,50.73, and 60.20 (JCPDS card No. (00.049.1642).[33] ZrO_2@S-doped g-C_3N_4 NCs have three major peaks encompassing ZrO_2 NPs and S-doped g-C_3N_4 NCs; no other phases were found. Figure 1 shows a peak intensity of ZrO_2 to grow with increasing ZrO_2 concentrations, while the peak intensity of S-doped g-C_3N_4 drops. This demonstrates effective integration of S-doped g-C_3N_4 with ZrO_2. As shown in Table 1, due to processing kinetics, particles of ZrO_2@S-doped g-C_3N_4 NCs evolved from agglomeration of small grains, acquiring a small crystal size. The average crystallite size (D) of each catalyst was calculated using Scherrer's formula (eq 1).

Table 1. Crystallite Sizes of Bulk g-C_3N_4, S-Doped g-C_3N_4, and ZrO_2@S-Doped g-C_3N_4 (ZrO_2 = 5, 10, 20, and 30%) NCs and Pure ZrO_2

material	2θ	FWHM (rad)	height	D (nm)
bulk g-C_3N_4	27.25	1.548	490	5.52
S-doped g-C_3N_4	23.98	0.641	481	13.23
ZrO_2@ S-doped g-C_3N_4 (5%)	26.53	1.550	273	5.50
ZrO_2@ S-doped g-C_3N_4 (10%)	27.26	1.296	546	6.59
ZrO_2@ S-doped g-C_3N_4 (20%)	35.97	1.249	527	6.99
ZrO_2@ S-doped g-C_3N_4 (30%)	35.75	1.277	544	6.83
pure ZrO_2 NPs	46.94	0.691	599	13.10

$$D = \frac{0.9\lambda}{\beta\cos\theta} \quad (1)$$

where D is the average particle size of the sample (nm), θ is the angle between the incident and diffracted beams (degree), β is the full width half-maximum (FWHM) of the peaks at diffracting angle and λ is the wavelength of the X-rays.

3.2. Functional Group Studies. The FT-IR spectra of bulk g-C_3N_4, S-doped g-C_3N_4, and ZrO_2@S-doped g-C_3N_4 (5, 10, 20, and 30%) NCs and ZrO_2 NPs are shown in Figure 2.

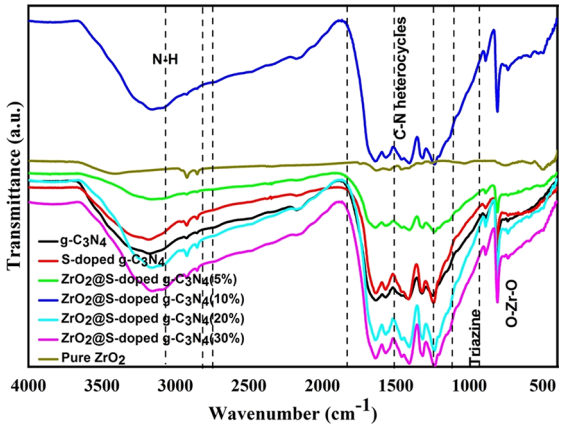

Figure 2. FTIR spectra of bulk g-C_3N_4, S-doped g-C_3N_4, and ZrO_2@S-doped g-C_3N_4 (5, 10, 20, and 30%) NCs and ZrO_2 NPs.

The chemical structure of bulk g-C_3N_4 and S-doped g-C_3N_4 displays a sharp absorption peak at 808 cm^{-1}, associated with *s*-triazine ring modes, and a strong absorption peak in the range of 1200−1700 cm^{-1}. The spectrum peak at 1645 cm^{-1} is attributable to C ≡ N stretching vibration modes. At the same time, the peaks at 1241, 1319, and 1404 cm^{-1} are due to aromatic C−N stretching. This is due to the bending vibration of the *tri-s*-triazine C−N bond. The broad peak at 3040−3302 cm^{-1} matches the broad absorption caused by an aromatic ring defect.[20] The hydroxyl groups on the surface of hydrated oxide together with adsorbed water generate the broad absorption peak at 3373 cm^{-1}. These features demonstrate the structural similarities of g-C_3N_4 and S-doped g-C_3N_4, although sulfur doping resulted in a small change in the band position for the

https://doi.org/10.1021/acsomega.2c08174
ACS Omega 2023, 8, 13775−13790

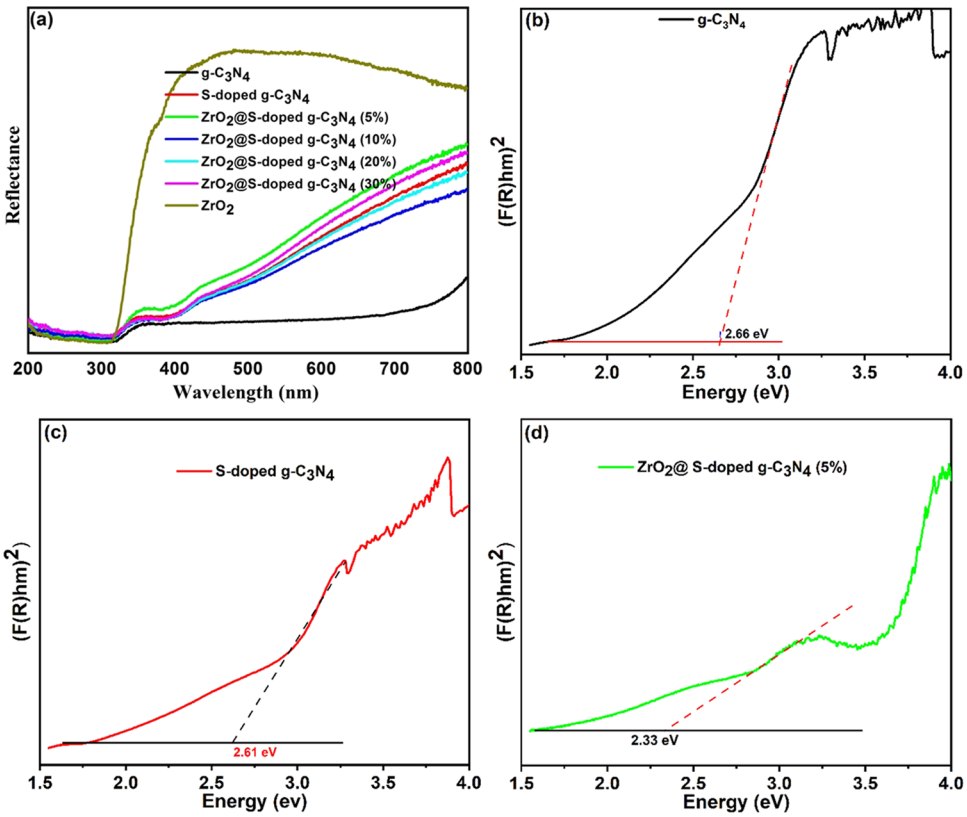

Figure 3. Diffuse reflectance absorption spectra of (a) g-C_3N_4, S-doped g-C_3N_4, ZrO_2@S-doped g-C_3N_4 (5, 10, 20, and 30%), and ZrO_2, and (b–d) optical band gap plots transformed by the Kubelka–Munk function of bulk g-C_3N_4, S-doped g-C_3N_4 and ZrO_2@S doped g-C_3N_4 (5%) NCs.

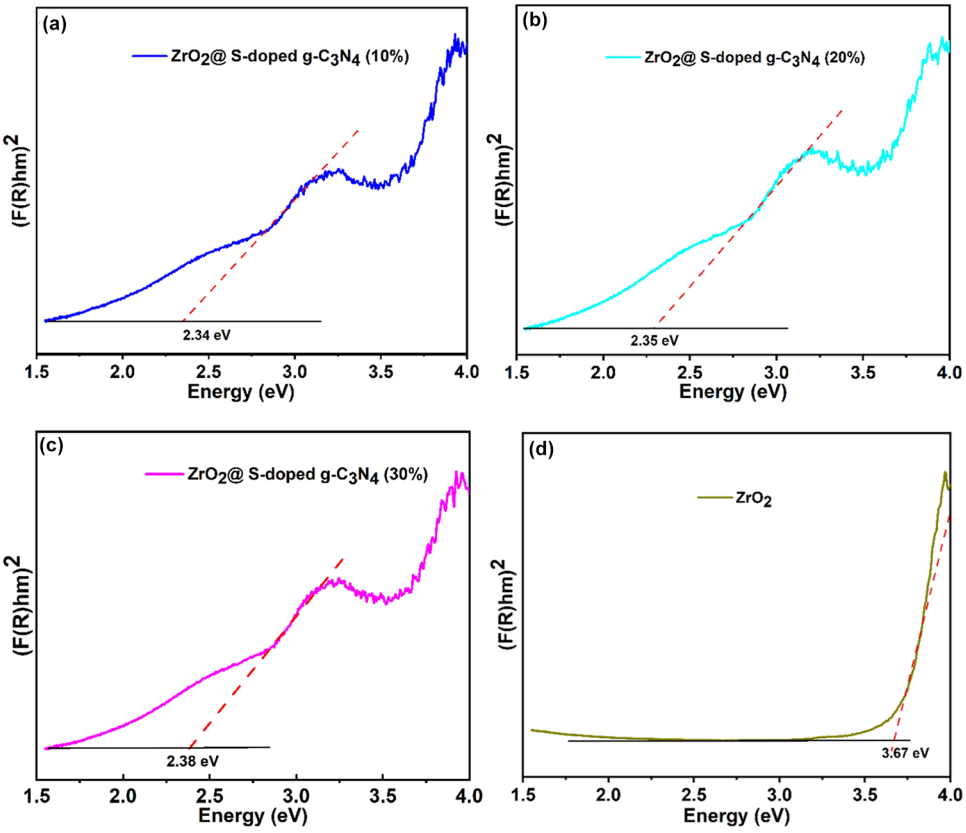

Figure 4. Optical band gap plots transformed by the Kubelka–Munk function (a–d) of ZrO_2@S doped g-C_3N_4 NCs and pure ZrO_2.

https://doi.org/10.1021/acsomega.2c08174
ACS Omega 2023, 8, 13775–13790

tri-substituted *tri*-*S*-triazine ring. In addition to the XRD (Figure 1) result, the corresponding shift suggests successful formation of S-doped g-C_3N_4.[35] As shown in Figure 2, the weak peak around 710 cm^{-1} appeared in the FT-IR spectrum of S-doped g-C_3N_4, demonstrating successful integration of sulfur into the g-C_3N_4 structure by substituting N with S atoms forming C−S chemical bonds in the structure of g-C_3N_4. This shows that S-doping does not change the skeleton structure of g-C_3N_4.

The stretching vibrations of Zr−O result in pure ZrO_2 absorption peaks at 509 and 750 cm^{-1}. The peak situated at 478 cm^{-1} is attributed to Zr−O vibrations.[20] With increasing ZrO_2 NPs, peak positions vary around 509 and 3373 cm^{-1}.[33] FT-IR of ZrO_2@S-doped g-C_3N_4 NCs is similar to that of pure phase S-doped g-C_3N_4.[33] While ZrO_2 has been added to the surface of S-doped g-C_3N_4, primary characteristic peaks of both S-doped g-C_3N_4 and ZrO_2 are visible. The FT-IR spectrum and XRD data agree with each other, proving that ZrO_2@S-doped g-C_3N_4 NCs were indeed formed.

3.3. Optical Property Study. To study the optical properties of the synthesized samples, UV−visible diffuse reflectance spectra (UV−vis DRS) of bulk g-C_3N_4, S-doped g-C_3N_4, and ZrO_2@S-doped g-C_3N_4 (5, 10, 20, and 30%) NCs and ZrO_2 NPs were obtained at room temperature between 200 and 800 nm. The tangent and horizontal line parallel to the abscissa are provided by the cut line method to determine the absorption wavelength threshold. The Kubelka-Munk equation was used to calculate optical band gap energies (E_g) for the prepared samples. This equation (eq 2) was used to determine diffused reflectance (R) and optical absorption coefficients (α),[43]

$$\alpha = \frac{(1-R)^2}{2R} \tag{2}$$

where R is the percentage of reflected light and α is the optical absorption coefficient of the semiconductor at a certain value of wavelength λ. To obtain E_g, the Kubelka-Munk function was used as represented by eq 3.

$$\alpha h\nu = A(h\nu - E_g)^n \tag{3}$$

where A is a constant that depends on the transition probability related to effective masses associated with the valence band and conduction bands, while n is the power index related to the optical absorption process, depending on transition characteristics in the semiconductor. The n value was chosen to be 1/2 for indirectly allowed transitions, h is Planck's constant, ν is the frequency of light, E_g stands for the energy gap between the bottom of the conduction band (C_B), and the top of the valence band (V_B).

Figures 3b−d and 4a−d, namely, the plots of $[F(R)h\nu)]^n$ vs $h\nu$, show the intercepts between the tangent and horizontal lines, lying between 2.66−3.67 eV for the direct band gaps (E_g/eV) from the Kubelka−Munk n (1/2) values. The calculated E_g values of NCs prepared from various ratios of ZrO_2 were approximately 2.33, 2.34, 2.35, and 3.38 eV for 5, 10, 20, and 30% of ZrO_2, respectively. The values were closer to the known values reported in the literature.[20,33] It was noticed that the ZrO_2@S-doped g-C_3N_4 NC has better light absorption properties than g-C_3N_4 and S-doped g-C_3N_4 and ZrO_2. It may be due to the synergistic effect between the interactions of ZrO_2 with S-doped g-C_3N_4. Thus, some chemical bonds formed between the two semiconductors (S-doped g-C_3N_4 and ZrO_2) may significantly decrease the E_g value, as depicted in Table 2. This offers more proof that the inclusion of ZrO_2 NPs enhances the optical properties of the S-doped g-C_3N_4 NC at a wider wavelength range.

Table 2. Experimental E_g Values Obtained for the Synthesized NCs

samples	$(F(R)h\nu)^{1/2}$ (eV)
pure g-C_3N_4	2.66
S-doped g-C_3N_4	2.61
ZrO_2@S-doped g-C_3N_4 (ZrO_2 = 5%)	2.33
ZrO_2@S-doped g-C_3N_4 (ZrO_2 = 10%)	2.34
ZrO_2@S-doped g-C_3N_4 (ZrO_2 = 20%)	2.35
ZrO_2@S-doped g-C_3N_4 (ZrO_2 = 30%)	2.38
pure ZrO_2	3.67

3.4. Photoluminescence Spectroscopy Analysis. The photoluminescence spectra of bulk g-C_3N_4, S-doped g-C_3N_4, and ZrO_2@S-doped g-C_3N_4 (5, 10, 20, and 30%) NCs and pure ZrO_2 NP are shown in Figure 5a. The effect of g-C_3N_4, S-doped g-C_3N_4, and ZrO_2 on ZrO_2@S-doped g-C_3N_4 NCs on the separation efficiency of electron−hole pairs was investigated. Pure ZrO_2 emits strongly at around 405 nm, which corresponds to its band gap transition emission. The energy of the light released is roughly equal to the band gap energy. When compared to pure ZrO_2 NPs, the intensity of fluorescence emission from ZrO_2@S-doped g-C_3N_4 NCs was observed to be dramatically reduced. Thus, when ZrO_2 NPs were added to S-doped g-C_3N_4, the degree of fluorescence quenching showed a significant enhancement. As a result, it

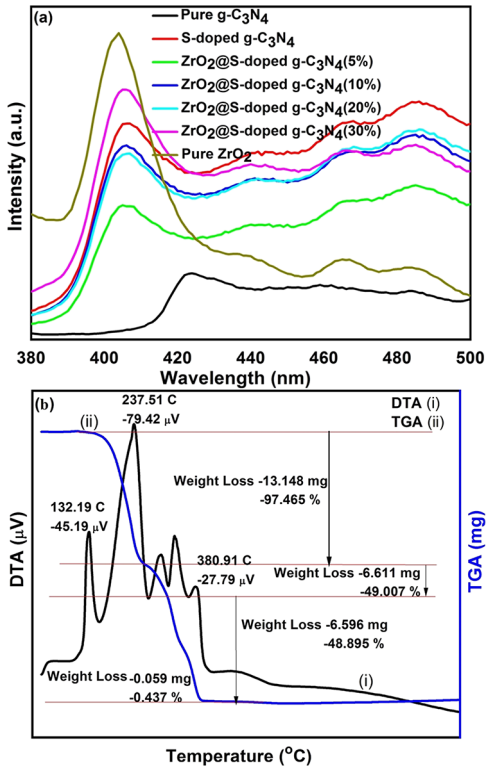

Figure 5. Photoluminescence spectra of (a) g-C_3N_4, S-doped g-C_3N_4, and ZrO_2@S-doped g-C_3N_4 (5, 10, 20, and 30%) NCs and pure ZrO_2, and (b) TGA/DTA thermogram for S-doped g-C_3N_4 NCs.

https://doi.org/10.1021/acsomega.2c08174
ACS Omega 2023, 8, 13775−13790

was shown that the electron−hole recombination rate increases initially, then declines among the ZrO_2@S-doped g-C_3N_4 (5, 10, 20, 30%) NCs, with the ZrO_2@S-doped g-C_3N_4 (5%) NC recombination rate being the lowest and the ZrO_2@S-doped g-C_3N_4 (30%) NC being the largest. On the other hand, ZrO_2@S-doped g-C_3N_4 (10 and 20%) NCs have a band similar to the quenched PL emission peak at approximately 486 nm. In contrast to g-C_3N_4 and pure ZrO_2, this reveals suppressed recombination of photogenerated charge carriers produced by doping with S. This implies that the synergistic effect between g-C_3N_4, S-doped g-C_3N_4, and ZrO_2 plays a big role in the optimum electron−hole recombination rate of ZrO_2@S doped g-C_3N_4 NCs. The optimum intensity of ZrO_2@S-doped g-C_3N_4 NCs suggests successful introduction of an impurity phase (S and ZrO_2) in ZrO_2@S-doped g-C_3N_4 compared to the lower g-C_3N_4 and higher ZrO_2 recombination rate of the photogenerated electrons and hole pairs, respectively.[21]

3.5. Thermal Stability Analysis. TGA/DTA analysis was employed to investigate the thermal degradation of the samples and stability under a N_2 atmosphere. TGA scans covered from room temperature to 1000 °C at a heating rate of 15 °C min^{-1} (Figure 5b). The TGA/DTA thermogram shows the change in the sample weight as a function of temperature under a controlled gas atmosphere (N_2) and temperature. From DTA (Figure 5b, black line), the dynamic relationship between temperature with change in physical or chemical processes and the percentage of weight change (gain or loss) over a programmed temperature is seen. From the DTA curve, endothermic transformations were observed at 132.19, 237.51, and 300.91 °C. The decomposition reaction of urea and ammonium sulfate that produces gases that exit and remove heat from the system is seen in the increase of the weight loss rate that rises to a maximum and takes place during isomerization.[44] Pyrolysis of urea and ammonium sulfate is the cause for an endothermic effect that forms S-doped g-C_3N_4 during the heating process.

The DTA shows two heat absorption peaks that were present during the initial phase of mass loss, supporting endothermic activity: first, the slow melting of the sample between 22.27 and 132.9 °C (representing melting rather than decomposition by the absence of any detected mass loss) and the first stage decomposition reaction up to 385 °C endothermic transformations. The pyrolysis of urea may cause weight loss and endothermic peaks. The second peak between 200 and 385 °C (about 97.465 wt % weight loss) observed in the TGA curve corresponds to further decomposition of urea and ammonium sulfate to form S-doped g-C_3N_4 during the heating process.

3.6. Morphology and Compositional Analysis. The HR-SEM analysis was mainly helpful in providing information about the surface morphologies of the samples obtained by chemical precipitation and calcination synthesis methods, as depicted in Figures 6 and 7. In this technique, elemental composition in the prepared samples' inner and outer surfaces was investigated. The magnified images of the size, shape, elemental composition, crystallography, and other physical and chemical features of bulk g-C_3N_4, S-doped g-C_3N_4, and ZrO_2@S-doped g-C_3N_4 NCs were examined. HR-SEM studies showed that the bulk g-C_3N_4 (Figure 6a,b), S-doped g-C_3N_4 (Figure 6c,d), and ZrO_2@S-doped g-C_3N_4 (Figure 6e,f) are agglomerated particles with irregular shape and varied packing density. The surface morphology of monoclinic-shaped ZrO_2 NPs comprises numerous non-uniform NPs with many pores

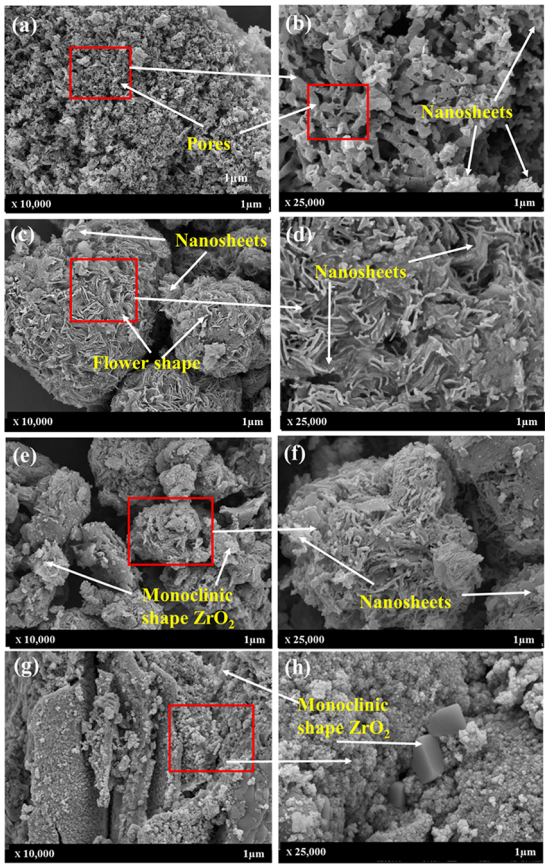

Figure 6. HR-SEM images of (a, b) bulk g-C_3N_4, (c, d) S-doped g-C_3N_4 (e, f), and ZrO_2@S-doped g-C_3N_4 NCs, and (g, h) ZrO_2 NPs with different magnifications.

and voids (Figure 6g,h). S-doped g-C_3N_4 and ZrO_2 are very different from one another in terms of morphology, ensuring ease of detection by scanning electron microscopy. The white irregular mass seen in Figure 6e,f contains ZrO_2 and is coated with flaky S-doped g-C_3N_4, demonstrating better integration.

The HR-SEM/EDS mappings (Figure 7a−f) revealed additional evidence for the presence of N, C, S, Zr, and O elements in the ZrO_2@S-doped g-C_3N_4 NC. Combined with XRD and FT-IR analysis, these findings demonstrate successful incorporation of ZrO_2 into the S-doped g-C_3N_4 host lattice.

3.7. Surface Area Analysis. The distribution of pore sizes and surface area of the synthesized samples were characterized by Brunauer−Emmett−Teller (BET) measurements. Figure 8a shows the nitrogen adsorption−desorption isotherm of g-C_3N_4, S-doped g-C_3N_4, ZrO_2@S-doped g-C_3N_4, and ZrO_2 samples, illustrating a typical type IV curve and the presence of mesoporous structured NCs with exception of bulk g-C_3N_4.

The nanoparticle hysteresis loop's shape is type H3, associated with bulk-like particles giving rise to narrow slit-shaped pores, which is consistent with the HR-SEM results (Figure 6). For bulk g-C_3N_4, larger adsorption capacity is found in the high-pressure range ($P/P^0 > 0.2$), indicating that it has mainly mesopores, while the other NCs achieve most of their N_2 adsorption between 0.5 and 1.0, indicating the presence of mesoporous structures formed by aggregation of NPs.[45,46] The decreased surface area after doping by S is attributed to the disappearance of the small pores but was gradually enhanced by adding additional small pores when ZrO_2 was confined within the S-doped g-C_3N_4 NC. Thus, the

https://doi.org/10.1021/acsomega.2c08174
ACS Omega 2023, 8, 13775−13790

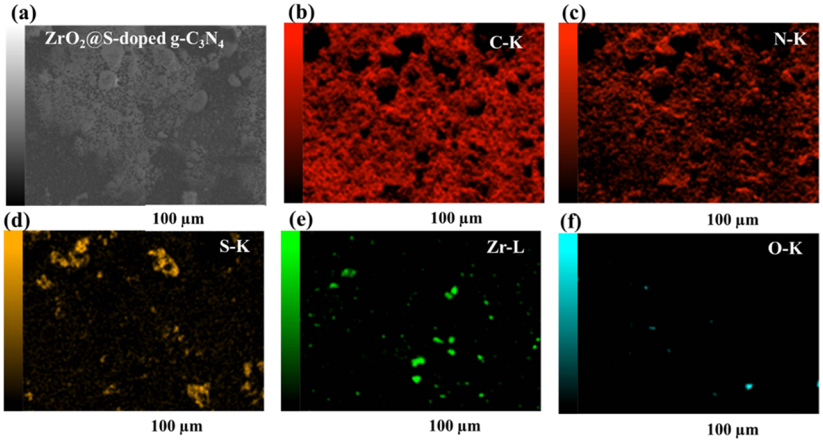

Figure 7. HR-SEM/EDS mapping (a) for ZrO_2@S-doped g-C_3N_4 NC and (b–f) constituent elements of the NCs.

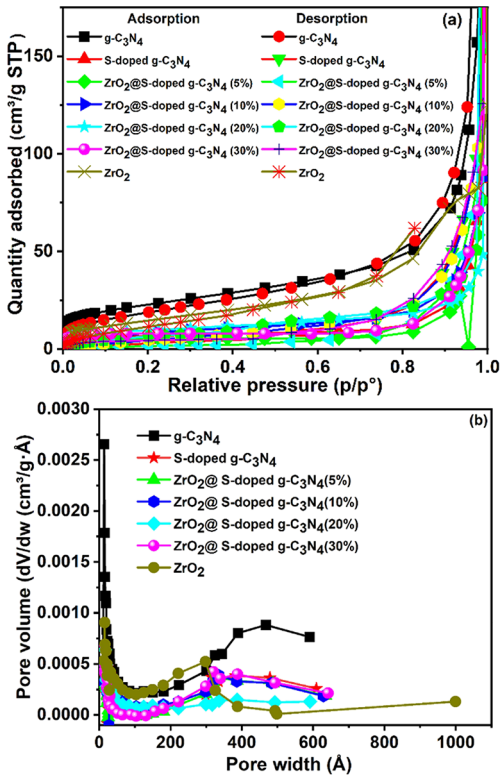

Figure 8. (a) N_2 adsorption–desorption isotherms and (b) pore size distributions of g-C_3N_4, S-doped g-C_3N_4, and ZrO_2@S-doped g-C_3N_4 NCs and ZrO_2.

S_{BET} of g-C_3N_4 decreases from 81.6 to 27 $m^2\ g^{-1}$ as the amount of ZrO_2 increases, arising from the high crystallinity of monoclinic ZrO_2 NPs. This is confirmed by pore size distribution, as shown in Table 3 and Figure 8b. At the same time, the BJH pore size and volume of ZrO_2@S-doped g-C_3N_4 NCs were also increased, implying cavities or tunnels developing in ZrO_2@S-doped g-C_3N_4 NCs. While the significantly lower pore size of ZrO_2@S-doped g-C_3N_4 (5, 10, and 30%) results from carcass construction, the higher pore size of ZrO_2@S-doped g-C_3N_4 (20%) NC arises from intracrystalline pores.[31]

The S_{BET} results illustrate that the enhanced performance of the ZrO_2@S-doped g-C_3N_4 (20%) NC is not only due to improved electron–hole recombination rate but also due to changes in the BET surface area. In general, ZrO_2@S-doped g-C_3N_4 NCs have appealing features such as a large specific surface area and a mesoporous structure, allowing for a higher degree of absorption, which may be beneficial for aqueous penetration in the electrocatalytic and adsorption reactions.

3.8. XPS Analysis. The XPS technique is widely used to characterize surface elemental composition and electronic states of NCs. As shown in Figure 9, the total XPS survey spectra of bulk g-C_3N_4 and S-doped g-C_3N_4 NCs clearly indicates the presence of C and N in g-C_3N_4. The C 1*s* and N 1*s* peaks around 288.1 and 398 eV correlate well with the reported values for g-C_3N_4.[22] The XPS survey spectrum of ZrO_2 NPs shows the presence of the bonds between Zr and O elements, which confirms successful synthesis of the ZrO_2@S-doped g-C_3N_4 NC.

High-resolution XPS spectra for C 1*s*, N 1*s*, and S 2*p* are presented in Figures S1 and S2. The N 1*s* peak of the ZrO_2@S-doped g-C_3N_4 NC was deconvoluted (Figure S3) into two fitted peaks at 398.0 and 399.2 eV. The results indicated that there are two distinct different chemical environments for the

Table 3. BET Surface Areas, Pore Size, and Pore Volume Distribution in the Prepared Samples

		pore volume ($cm^3\ g^{-1}$)		pore size (nm)	
samples	S_{BET} (m^2g^{-1})	BJH adsorption	BJH desorption	BJH adsorption	BJH desorption
g-C_3N_4	81.6	0.33	0.75	12.7	35.9
S-doped g-C_3N_4	24.4	0.13	0.24	15.1	23.5
ZrO_2@S-doped g-C_3N_4 (5%)	21.3	0.12	0.14	12.8	22.3
ZrO_2@S-doped g-C_3N_4 (10%)	28.7	0.13	0.16	12.4	17.2
ZrO_2@S-doped g-C_3N_4 (20%)	35.6	0.07	0.07	5.4	9.0
ZrO_2@S-doped g-C_3N_4 (30%)	27.7	0.14	0.19	12.5	19.1
pure ZrO_2	56.3	0.19	0.13	10.0	7.4

https://doi.org/10.1021/acsomega.2c08174
ACS Omega 2023, 8, 13775–13790

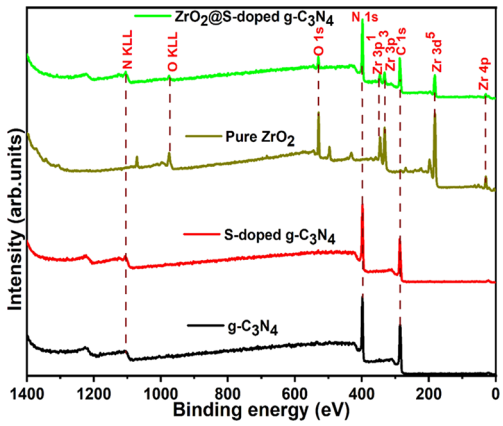

Figure 9. XPS survey spectra for pure g-C_3N_4, S-doped g-C_3N_4, pure ZrO_2, and ZrO_2@S-g-C_3N_4.

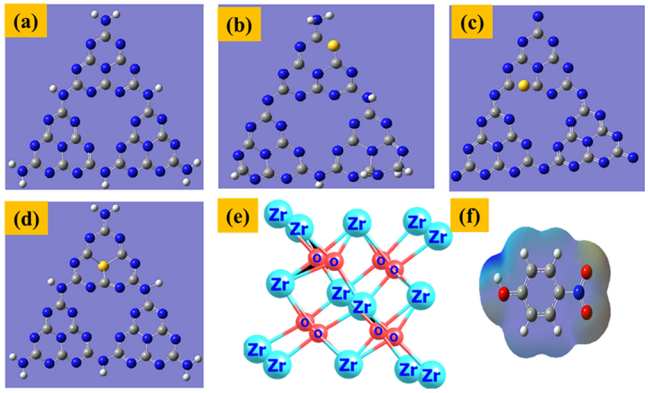

Figure 11. Molecular orbital energies and structures of (a) pure g-C_3N_4, (b) S-doped g-C_3N_4 with nitrogen (N_1) substituted by sulfur at site 1, (c) S-doped g-C_3N_4 with nitrogen (N_2) substituted by sulfur at site 2, (d) S-doped g-C_3N_4 with nitrogen (N_3) substituted by sulfur at site 3, (e) cubic ZrO_2, and (f) ESP mapping of the optimized 4-NP. Color coding: gray C, blue N, yellow S, red oxygen, and white hydrogen.

nitrogen atoms of ZrO_2@S-g-C_3N_4. The predominant peak at a binding energy of 398.0 eV was assigned to the pyridine sp^2 hybridized N atom (−C−N═C−), while the peak at 399.2 eV was attributed to the sp^3 hybridized N atom, N(−C)$_3$. In the XPS spectra of S-doped g-C_3N_4 for S 2*p*, the peak around 164.2 eV was assigned to C−S. The C 1*s* spectrum shown in Figure S2b confirms the existence of bonds between C−S−C with peaks around 285.5−287.5 eV. This analysis is in agreement with the previous reports.[21,47]

In the XPS spectrum (Figure 10a), the presence of two peaks centered at 181.7 and 184.1 eV are attributed to Zr $3d_{5/2}$ and Zr $3d_{3/2}$, respectively, for ZrO_2@S-doped g-C_3N_4 NCs. In addition, the O 1*s* peak around 529.9 eV, as shown in Figure 10b, was assigned to the Zr−O bonds related to the O_2^- ions in monoclinic ZrO_2.[48] Based on HRSEM, FTIR, XRD, and XPS results, it is concluded that the ZrO_2@S-doped g-C_3N_4 NC electrocatalyst had been successfully prepared.

3.9. Computational Studies. We compared the experimental and predicted band gaps using DFT calculations to provide more clarity on the precise substitution positions of S. From the N 1*s* XPS analysis of g-C_3N_4, it was pointed out that there are three types of N atoms.[21,47] As such, an atomic structure model of pure g-C_3N_4 composed of melon units (*S*-triazine) was constructed (Figure 11). In this model, three types of the melon system were constructed and the N atoms were numbered as N_1, N_2, and N_3, based on their positions for S substitution. Calculations were performed for three types of S-doped g-C_3N_4 models and the band gaps for S-substituted melon systems were found to be 1.70, 1.68, and 1.16 eV for N_1 (−C−N═C−), N_2 (−C═N−C−), and N_3 (N(−C)$_3$)-substituted melon systems, respectively. It is important to note that DFT underestimates band gaps compared to experimental results.[3] Furthermore, the doping circumstances, structural models, type of basis sets, and DFT functionals were also found to affect E_g values. When compared to the pattern seen in the calculated band gaps, the band gap for the structure with S doping at position N_1 (Figure 11b) agrees with the experimental band gap than the other two. The −C−S−C− bond that resulted when S is substituted for N_1 is in good agreement with the findings of the S 2*p* XPS survey of the S-doped g-C_3N_4 NC, which indicated the presence of the −C−S−C− bond at 164.2 eV. On the other hand, since S is a larger atom than N and C, it was found that replacing N_3 with S for optimized geometries resulted in significant lattice distortion, which also changed the E_g values, while replacing N with S in the other two cases did not result in significant structural distortion, which is consistent with a previous study.[16]

3.10. Electrochemical Studies of ZrO_2@S-Doped g-C_3N_4/FTO. *3.10.1. Electrochemical Characterizations of the Modified Electrodes.* The electrochemical behavior of bare g-C_3N_4/FTOE, S-doped g-C_3N_4/FTOE, ZrO_2@S-doped g-C_3N_4/FTOE, pure ZrO_2/FTOE, and FTO was investigated using a 0.1 M KCl 5 mM $Fe(CN)_6^{3-/4-}$ redox probe electrolyte solution at a scan rate of 50 mV^{-1}. The results

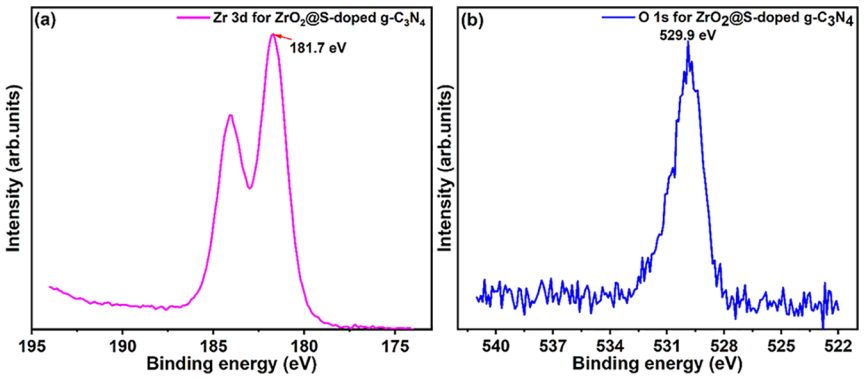

Figure 10. XPS high-resolution spectra of (a) monoclinic zirconia Zr 3*d* and (b) O 1*s* peaks for the ZrO_2@S-doped g-C_3N_4 NC.

https://doi.org/10.1021/acsomega.2c08174
ACS Omega 2023, 8, 13775−13790

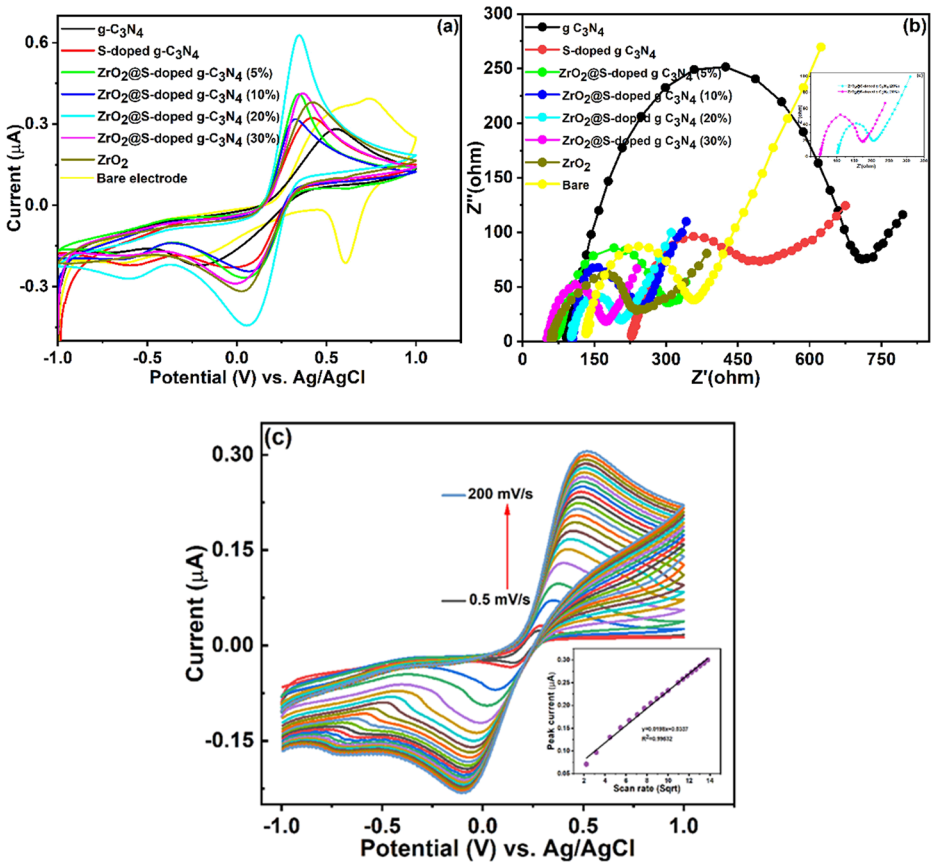

Figure 12. Electrochemical characterization of pure g-C_3N_4, S-doped g-C_3N_4 NCs, ZrO_2@S-doped g-C_3N_4, pure ZrO_2, and bare electrode using (a) CV measurements, (b) EIS Nyquist plots where the inset is the EIS Nyquist plot for ZrO_2@S-doped g-C_3N_4 (20 and 30%) (0.1 M KCl; 5 mM $Fe(CN)_6^{3-/4-}$ scan rate = 50 mV s^{-1}, and (c) different scan rates (0.5−200 mV s^{-1}) for ZrO_2@S-doped g-C_3N_4 (20%)/FTO.

are presented in Figure 12. Figure 12a shows the modified ZrO_2@S-doped g-C_3N_4(20%)/FTOE exhibiting a well-defined redox peak with a high electron transfer capability compared to g-C_3N_4, S-doped g-C_3N_4 NCs, ZrO_2@S-doped g-C_3N_4(5, 10, and 30%)/FTOE, and bare FTOE. The g-C_3N_4/FTOE shows low electron transfer in comparison with other electrodes. This is due to its poor electrical conductivity, which limits the electron transfer probe of $Fe(CN)_6^{3-/4-}$ on the surface of the FTOE. The insulating behavior of g-C_3N_4 might have blocked diffusion of the redox probe and increased internal resistance at the electrode interfaces, as shown in Figure 12b. Nevertheless, the ZrO_2@S-doped g-C_3N_4(20%)/FTOE NC shows a well-defined peak current, which gave efficient electron transfer capability, enhanced electrical conductivity, and large surface area of the NCs.

On the other hand, electrochemical impedance spectroscopy (EIS) is a very helpful tool to characterize layered and composite nanomaterials. Figure 12b presents the EIS plots of the bare g-C_3N_4, S-doped g-C_3N_4 NCs, ZrO_2@S-doped g-C_3N_4 (5, 10, 20, and 30%) NCs, pure ZrO_2, and bare electrode, which were recorded to determine double layer capacitance or conductivity in the presence of a 0.1 M KCl and 5 mM $Fe(CN)_6^{3-/4-}$ redox probe. In the middle frequency region, the semicircle is correlated with interfacial charge transfer resistance (R_{ct}). The smallest semicircle (Figure 12b Inset) indicates the fastest interfacial electron transfer and efficient separation of electron−hole pairs, which was often related to intraparticle and interparticle resistance.[49] The ZrO_2@S-doped g-C_3N_4 (20%) NC gave the smallest semicircle, implying faster interfacial electron transfer than that of pure ZrO_2, g-C_3N_4, S-doped g-C_3N_4, ZrO_2@S-doped g-C_3N_4 (5, 10, and 30%), and bare FTOE. It is important to note that the ZrO_2@S-doped g-C_3N_4 (20%)/FTOE exhibited a redox current higher than 30%. This is mainly due to its optimal electron hole recombination rate, outstanding electrical conductivity property, and larger surface area of the NCs than those of ZrO_2@S-doped g-C_3N_4(30%)/FTOE). Overall, the results showed the surface properties and introduction of sulfur and zirconia (ZrO_2) as a dopant into the lattice of g-C_3N_4, which have been believed to have played a vital role in the electrochemical performance. This evidence revealed that there was a combination of charge carriers. For this reason, ZrO_2@S-doped g-C_3N_4 (20%) NC was selected for additional electrochemical sensing studies of 4-NP.

The relation between peak current and the scan rate for ZrO_2@S-doped g-C_3N_4 (20%)/FTO is presented in Figure 12c, and the effect of the scan rate in the presence of 4-NP is presented in Figure S4. Furthermore, to evaluate the molecular diffusion on the surface of the modified electrode, a calibration curve was plotted between the peak current and the square root of the scan rate within the 0.5−200 mVs^{-1} range, using 0.1 M KCl 5 mM $Fe(CN)_6^{3-/4-}$ (Figure 12c inset). The increase in redox peak current shows that the electrocatalytic activity was successfully improved at the surface of the modified electrode. In this regard, the peak current has grown linearly with the square root of the potential scan rate. The plots of anodic peak current (I_{pa}) and cathodic peak current (I_{pc}) versus the square root of the scan rate $(SR)^{1/2}$ further

https://doi.org/10.1021/acsomega.2c08174
ACS Omega 2023, 8, 13775−13790

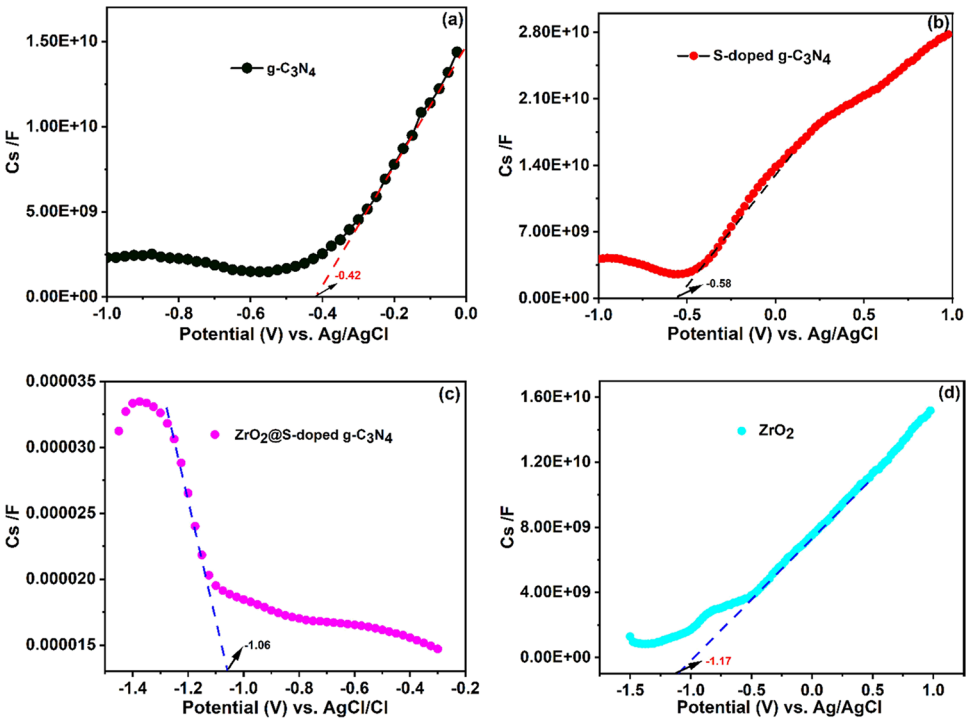

Figure 13. Mott−Schottky curve for (a) g-C_3N_4, (b) S-doped g-C_3N_4, (c) ZrO_2@S-doped g-C_3N_4, and (d) ZrO_2 at a frequency of 1000 Hz in the dark.

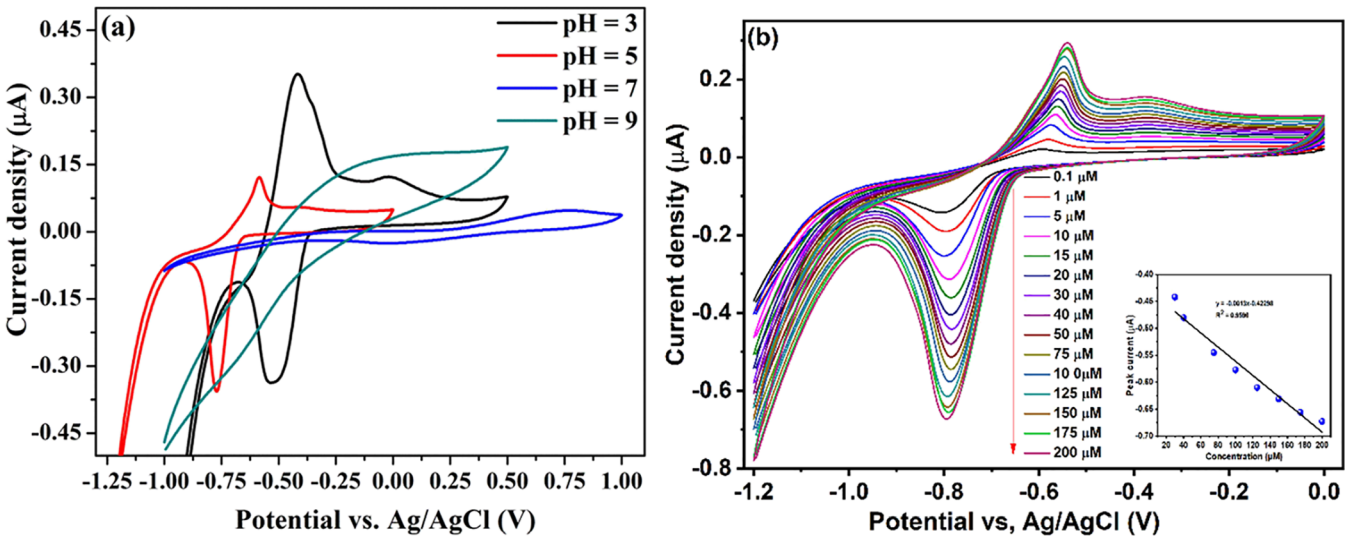

Figure 14. Cyclic voltammograms for ZrO_2@S-doped g-C_3N_4 (20%)/FTO under different conditions of (a) pH and (b) concentrations of 4-NP at a range of 0.1 μM − 200 μM. Inset in (b) depicts the calibration plot for 4-NP concentration against peak current (0.1 M PBS, pH 5.0 and scan rate of 50 mV s^{-1}).

support the linear relationship of both oxidation and reduction processes against the square root of the scan rate (see Figure S5). The plots gave the following linear relations:

$$I_{pc} = 0.017(SR)^{1/2} - 0.0954 \quad (4)$$

$$I_{pa} = -0.01325(SR)^{1/2} - 0.0628 \quad (5)$$

A previous study also reported similar observations.[2] The electrochemical area of the bare electrode was 0.0241cm^2, whereas the active surface area of the modified electrode was calculated from the slope of the peak current versus $V^{1/2}$ plot and was found to be 0.1327 cm^2. On the other hand, the sensitivity of the modified electrode was calculated to be 4.9 μA mM^{-1} cm^{-2}. Results indicate that detection was governed by a diffusion-controlled process, again in agreement with previous studies.[50,51]

3.10.2. Mott−Schottky Analysis. Mott-Schottky (M-S) measurements were conducted to determine the flat band potential values and electronic band structure shifts in 0.5 M Na_2SO_4 in the absence of light (Figure 13a−d). The positive slope of the tangent lines in Figure 13a,b,d indicates that g-C_3N_4, S-doped g-C_3N_4 NCs, and pure ZrO_2 NP are n-type semiconductors. For ZrO_2@S-doped g-C_3N_4 a typical p-type semiconductor with a negative slope was observed (Figure

https://doi.org/10.1021/acsomega.2c08174
ACS Omega 2023, 8, 13775−13790

13c). Its highest valence band (VB) potential could be estimated from its flat-band potential.[52] By using the Nernst equation (eq 6), the measured potentials may be converted to the reversible hydrogen electrode (RHE) scale:

$$E_{RHE} = E_{Ag/AgCl} + 0.05916\,pH + E^{0}_{Ag/AgCl} \quad (6)$$

where E_{RHE} is the converted potential vs RHE, $E_{Ag/AgCl}$ is the experimental potential measured against the Ag/AgCl reference electrode, and $E^{0}_{Ag/AgCl}$ refers to the standard potential of Ag/AgCl at 298 K (0.1976 V). The calculated conduction band edges of g-C_3N_4, S-doped g-C_3N_4, and ZrO_2 were found to be 0.19, 0.03, and −0.56 eV, respectively, while the valence band for ZrO_2@S-doped g-C_3N_4 was found to be −0.45 eV. As a result, the difference in V_{fb} (the shift of the Fermi level) causes the electric field to form over the heterojunctions at the interface between g-C_3N_4, S-doped g-C_3N_4, and ZrO_2 semiconductors. In the meantime, the balance of the Fermi level between g-C_3N_4, S-doped g-C_3N_4, and ZrO_2 can be formed because of the movement of electrons and holes. Since V_B and C_B have changed, the overall optical gap energy for ZrO_2@S-doped g-C_3N_4 decreased as a result.

The electron shift from V_B to C_B will modify both the energy and the momentum, which is a characteristic of an indirect band semiconductor. This assumption was made based on the explanation shown in Figure S6, namely that sulfur and zirconia doping had a major impact on the C_B and V_B edge. Consequently, the built-in electric field of the heterojunctions efficiently simplified the separation of electrons and holes and ultimately enhances the electrocatalytic performance of ZrO_2@S-doped g-C_3N_4 NC heterojunctions.[53]

3.10.3. Electrochemical Behaviors of 4-NP at the Modified Electrode. The cyclic voltammograms of the bare electrode (FTOE), g-C_3N_4/FTOE, S-doped g-C_3N_4/FTOE, ZrO_2/FTOE, and ZrO_2@S-doped g-C_3N_4(20%)/FTO were investigated with and without the use of 5 mM 4-NP in PBS (pH = 5.0) at the scan rate of 50 mV/s. In contrast to the modified electrodes, the unmodified FTOE does not show the reduction peak of 4-NP (Figure S7a). However, as shown in Figure 14 (vide infra), the designed sensor (ZrO_2@S-doped g-C_3N_4(20%)/FTOE) shows an improved electrocatalytic reduction behavior for 4-NP at the potential around −0.7958 V. It is inferred that ZrO_2@S-doped g-C_3N_4(20%)/FTOE displayed the best current response compared to other electrodes in the presence of the analyte (Figure S7). This is due to the existence of excellent synergy between S-doped g-C_3N_4 and ZrO_2, which facilitates the electrocatalytic ability of the nanocomposite. In this regard, S-doped g-C_3N_4 acts as a support for ZrO_2, while the existence of numerous pores, like in the nanosheets of S-doped g-C_3N_4, provides additional catalytic sites for 4-NP detection. It is important to note that under similar experimental conditions and in the absence of 4-NP, no peak was observed (Figure S7e). Thus, the ZrO_2@S-doped g-C_3N_4 (20%) NC-fabricated electrode was found to be the best sensor for 4-NP. Previous studies on 4-NP sensors also show that the current response of NCs significantly changes when 4-NP is being adsorbed.[5]

3.10.4. Optimization of Electrochemical Parameters. Typically, experimental parameters significantly influence electrochemical redox reactions. To increase the sensitivity of the electrochemical sensor, some experimental parameters such as pH and 4-NP concentration were optimized using 0.01 g of ZrO_2@S-doped g-C_3N_4(20%)/FTOE. For the detection of 4-NP, the ZrO_2@S-doped g-C_3N_4(20%)/FTO was used in aqueous media at room temperature conditions.

3.10.4.1. Effect of pH. There are controversies among researchers regarding the effect of acidic and alkaline environments on redox processes. A few authors concluded that acidic pH is favorable for the redox reactions of phenolic and nitro compounds, whereas some researchers reported alkaline pH as favorable for redox reactions. Hence, we studied the electrochemical behavior of ZrO_2@S-doped g-C_3N_4/FTOE by using cyclic voltammetry in 0.1 M PBS, 0.5 mM 4-NP, and 0.01 g NC and a pH of 3, 5, 7, and 9 at 50 mV s^{-1} scan rate (Figure 14a).

The strong pH-dependent property of the ZrO_2@S-doped g-C_3N_4 (20%)/FTOE reveals the involvement of proton-accessible species. This study showed that the stability of the designed sensor was pH-dependent, with highest stability under acidic conditions. At alkaline pH, the OH group concentration in the electrolyte solution increases. Since 4-NP also contains a hydroxyl group, it is possible that intermediate polymer products may form by reaction with OH groups in 4-NP and the surrounding environment. The formation of these polymeric intermediates could create a barrier for the flow of electrons during the electrochemical reaction of 4-NP. Hence, acidic environment is more favorable for the redox reactions of 4-NP than alkaline pH, in agreement with previous reports.[50,54] The higher reduction peak current may be due to electrostatic attraction between 4-NP and ZrO_2@S-doped g-C_3N_4 (20%). Thus, pH 5 was chosen for further 4-NP detection studies.

3.10.4.2. Effect of 4-NP Concentration. The response of ZrO_2@S-doped g-C_3N_4 (20%)/FTO toward detecting 4-NP at different concentrations was recorded, and the results are presented in Figure 14b. The CVs were recorded at different concentrations (0.1−200 μM) of 4-NP in 0.1 M PBS and a scan rate of 50 mV s^{-1} over the potential range of −1.2 to 0.0 V. Current change was monitored as a function of 4-NP concentration using ZrO_2@S-doped g-C_3N_4/FTOE as the sensor. The results revealed that the current response increases with increasing concentration of 4-NP. By taking the current at a higher point (0.673 μA), a calibration curve of the peak current against 4-NP concentration was plotted (Inset of Figure 14b), pertaining to ZrO_2@S-doped g-C_3N_4 (20%)/FTOE. Additionally, it was noted that there is no peak position shift between the CV plot for pH = 5 (Figure 14a) and that of the concentration dependence analysis (see Figure S8). The results suggest that ZrO_2@S-doped g-C_3N_4(20%)/FTOE is a very promising candidate as a sensor for detection of 4-NP.

3.10.5. Differential Pulse Voltammetry Determination of 4-NP. The electrochemical performance of the modified ZrO_2@S-doped g-C_3N_4 (20%)/FTOE for the estimation of 4-NP at pH 5 in 0.1 M of PBS was evaluated by DPV as it is very sensitive and selective method. Figure 15 shows the representative DPV responses corresponding to the reduction of various concentrations of 4-NP from 0.1 μ to 5 mM. The sensor parameters such as sensitivity (7.8892 $\mu A \mu M^{-1}$ cm^{-2}) were calculated from the slope of the LDR (0.2493 $\mu A \mu M^{-1}$) by considering the apparent surface area of the FTO (1cm^2). The result indicates that the peak current gradually increases upon successive 4-NP additions. The calibration plot of the reduction peak current vs concentration of 4-NP is shown in Figure 15. The inset plot indicates dependence of peak current on 4-NP concentration. It shows differential pulse voltammograms of 4-NP with concentrations ranging from 10 to 100 μM under optimized experimental conditions. The linear regres-

https://doi.org/10.1021/acsomega.2c08174
ACS Omega 2023, 8, 13775−13790

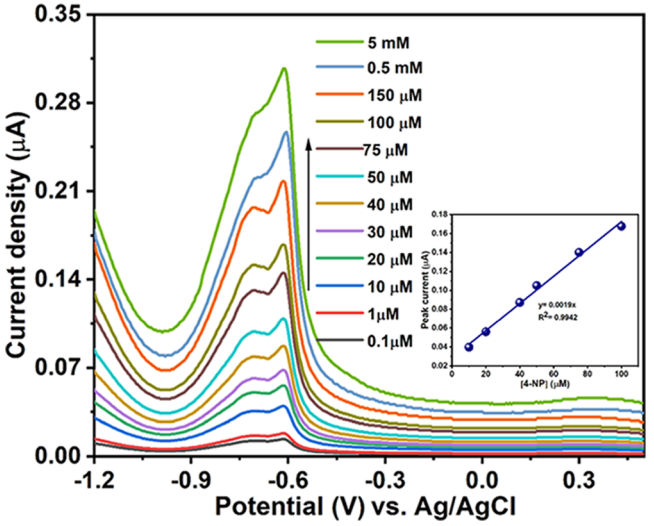

Figure 15. Differential pulse voltammograms at different concentrations (from 0.1 μM to 5 μM) of 4-NP at the ZrO_2@S-doped g-C_3N_4 (20%)/FTOE, with experimental conditions of pulse amplitude 50 mV, pulse width 50 ms, pulse period 0.1 s, potential range −1.2 to 0.6 V, and scan rate 50 mV s^{-1}. Inset: calibration plot for ZrO_2@S-doped g-C_3N_4 (20%) NCs.

sion equation is I_{pa} (μA) = 0.02837 × C (μM), with a correlation coefficient of 0.980. When using ZrO_2@S-doped g-C_3N_4 (20%)/FTO as the sensor, LOD is an essential parameter to consider. Toward detection of 4-NP, DPV data was further analyzed and the LOD was calculated using equations reported elsewhere. In Figure 15, the inset shows differential pulse voltammograms vs different concentrations of 4-NP at ZrO_2@S-doped g-C_3N_4 (20%)/FTOE in 0.1 M PBS (pH = 5.0). The LOD of 4-NP was calculated from the slope value of the calibration plot according to eq 7.

$$\text{LOD} = 3 \times \sigma / S \tag{7}$$

where σ is the standard deviation and S is the slope of the calibration curve. As a result, the newly developed ZrO_2@S-doped g-C_3N_4 (20%)/FTOE exhibited a low detection limit and excellent sensitivity of 6.654 μM. Thus, the DPV technique offered satisfactory analytical electroactive catalytic performance for detecting 4-NP. The analytical performance of the ZrO_2@S-doped g-C_3N_4 (20%)/FTOE was compared with that of different modified electrodes reported in recent days. Results are summarized in Table 4.

Although the electrodes listed in Table 4 are chemically modified glassy carbon electrodes and have lower detection limits than what is reported here, most of them have a smaller linear range than that of ZrO_2@S-doped g-C_3N_4(20%)/FTOE, indicating that the ZrO_2@S-doped g-C_3N_4/FTOE has a wider application range. In addition, even though Ag@Co-Al/PoPD/GCE exhibited outstanding performance with a wider linear range and lower detection limit,[54] the hydrothermal synthesis method is more complicated with multiple and longer time steps than the simple co-precipitation method applied in the preparation of ZrO_2@S-doped g-C_3N_4/FTO. The comparison shows ZrO_2@S-doped g-C_3N_4(20%)/FTOE to provide the best platform for 4-NP examination reported to date.

The plausible mechanism for the detection and reduction of 4-NP, as shown in Scheme 2, indicates that the process takes

Scheme 2. Proposed Mechanism for 4-NP Reduction on the ZrO_2@S-Doped g-C_3N_4(20%)/FTO Modified Electrode

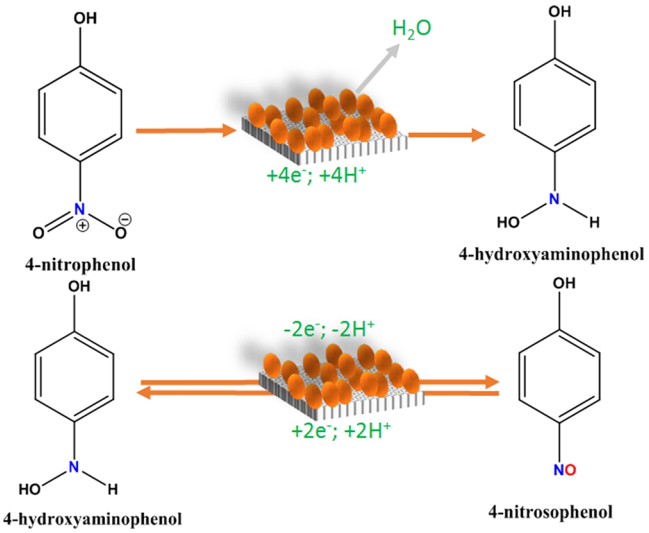

place on the surface of the modified electrode (Figure 15). The first step (broad peak of DPV) is the result of four-electron reduction of 4-NP to *p*-hydroxylaminophenol. *p*-hydroxylaminophenol then simply undertakes a two-electron oxidation process to give *p*-nitrosophenol. On the second narrow peak, *p*-nitrosophenol is then reduced through a reversible two-electron process back to *p*-hydroxylaminophenol producing the redox couple. This is in line with previously reported mechanisms for the reduction of 4-NP using a silver-decorated glassy carbon electrode and graphene oxide−TiO_2 composite.[50,57]

Based on this proposed reaction mechanism, the electrochemical redox reaction using ZrO_2@S-doped g-C_3N_4(20%)/FTOE in the presence of 4-NP can be expressed by the following four steps:

Table 4. Comparison of the Reported Electrochemical Procedures for Determination of 4-NP Using ZrO_2@S-Doped g-C_3N_4 (20%)/FTOE

modified electrode	detection method	linear range (μM/nM)	correlation coefficient	detection limit (μM/nM)	ref.
bio-synthesized CuO NPs	SWV	10 nM−10 mM	0.992	0.10 nM	6
RGO/Fe_3O_4NPs/GCENP[a]	DPV	0.2−10	0.9983	0.26 μM	55
TLISS/GCE[b]	DPV	1.43−55.93	0.9914	1.09 μM	4
Ag@Co-Al/PoPD/GCE[c]	DPV	0.82 × 10^{-9}−1.74 × 10^{-6} M	0.9990	63.70 nM	54
Nano-Au/GCE	LSV	10−100		8.00 μM	56
ZrO_2@S-doped g-C_3N_4/FTO	DPV	10−100	0.9798	6.65 μM	this work

[a]Reduced graphene oxide/Fe_3O_4 nanoparticle glassy carbon electrode. [b]Tremella-like indium silver sulfide glassy carbon electrode. [c]Ag nanoparticle-decorated Co-Al LDHs; Co-Al layered double hydroxides (LDHs), Co-Al LDHs/poly(*o*-phenylenediamine) (PoPD).

https://doi.org/10.1021/acsomega.2c08174
ACS Omega 2023, 8, 13775−13790

1st step: Mass transport of 4-NP from bulk solution to the ZrO_2@S-doped g-C_3N_4(20%)/FTO electrode surface,

2nd step: Adsorption of 4-NP on ZrO_2@S-doped g-C_3N_4(20%)/FTO through hydrogen bonding or electrostatic and π-π interactions,

3rd step: Electron transfer reaction takes place between the bulk solution and the modified electrode, on the surface of the electrode.

4th step: Mass transportation of the product from the ZrO_2@S-doped g-C_3N_4 (20%)/FTO surface into the bulk solution.

3.10.6. Reproducibility and Repeatability of ZrO_2@S-Doped g-C_3N_4/FTOE. To investigate the reproducibility of ZrO_2@S-doped g-C_3N_4 (20%)/FTO, four uniformly modified electrodes were fabricated under similar conditions. The response of 5 μM 4-NP was measured for the modified electrodes. The relative standard deviation (RSD) was found to be 3.19%. This RSD value indicates the modified electrode to sustain good reproducibility. The repeatability of the ZrO_2@S-doped g-C_3N_4(20%)/FTOE was tested by performing DPV for 7 measurements consecutively in 5 μM 4-NP. The relative standard deviations (RSD) of the anodic currents were calculated to be 3.6%, which shows appropriate repeatability of the ZrO_2@S-doped g-C_3N_4/FTO sensor for determining 4-NP. To determine stability, ZrO_2@S-doped g-C_3N_4 (20%)/FTO was repeatedly used to measure 5 μM 4-NP for 25 days and varying time periods (5 days, 1 week, 2 weeks, and 3 weeks). The modified electrode was kept in a refrigerator at 5 °C when not in use. The results are presented in Figure S9. The results show the cathodic peak current of 4-NP to still be at 99.1% after five days, while dropping to 97.2 and 95.8% after 1 week and 2 weeks, respectively. From all these results, it is evident that the ZrO_2@S-doped g-C_3N_4 (20%)/FTO-modified electrode possess excellent selectivity, repeatability, and stability, which make it suitable for the intended applications.

4. CONCLUSIONS

Using straightforward chemical precipitation and calcination techniques, ZrO_2@S-doped g-C_3N_4 was successfully synthesized. Chemical structures, pore sizes, morphology, crystalline structure, photoluminescence, formation energy and charge, and band gap analyses were performed by various experimental techniques. The electrochemical characteristics of the modified electrodes were examined using CV, EIS Nyquist, and Mott-Schottky measurements. Optimization and control growth of the existing ZrO_2@S-doped g-C_3N_4/FTOE as a sensor showed excellent ability for the detection of 4-NP. ZrO_2@S-doped g-C_3N_4 (20%) exhibited better detection of 4-NP compared to g-C_3N_4, S-doped g-C_3N_4, and ZrO_2@S-doped g-C_3N_4 (5, 10, and 30%) NCs and pure ZrO_2 NPs. This is ascribed to the fact that S-doped g-C_3N_4 and 20% ZrO_2 combined together improve electrocatalytic activity by lowering charge transfer resistance, while effectively suppressing electron−hole pair recombination. This is the consequence of desirable characteristics such as a large specific surface area, a mesoporous structure that allows for better absorption, moderate PL spectra, and EIS Nyquist and Mott-Schottky properties. The results indicated that the significant specific surface area and efficient electron−hole separation of ZrO_2@S-doped g-C_3N_4(20%) are due to synergistic effects among S-doped g-C_3N_4 and ZrO_2. A drop-cast technique was used to modify the binder-free ZrO_2@S-doped g-C_3N_4 electrode, which was attached to FTO. Successful detection of 4-NP was performed in an acidic medium (pH = 5). This demonstrated great sensitivity, low detection limit (6.65 M), and linear dynamic range (10−100 M) for the chosen electrochemical method at 298 K to detect 4-NP. To the best of our knowledge, the present work is the first report on detection of 4-NP with binder-free ZrO_2@S-doped g-C_3N_4 NCs using CV and DPV methods. The prepared NCs were found to be effective candidates for showing positive analytical results in environmental remediation against dangerous contaminants such as 4-NP for real-world applications.

■ ASSOCIATED CONTENT

Supporting Information

The Supporting Information is available free of charge at https://pubs.acs.org/doi/10.1021/acsomega.2c08174.

XPS survey, deconvoluted high-resolution spectra; effect of scan rate, plot of current versus square root of scan rate; comparison between postulated band structures; CV curves with and without 4-NP, and stability study (PDF)

■ AUTHOR INFORMATION

Corresponding Authors

Nigussie Alebachew − *Department of Applied Chemistry, School of Applied Natural Science, Adama Science and Technology University, Adama 251, Ethiopia*; Email: nigussiealebachew@gmail.com

H. C. Ananda Murthy − *Department of Applied Chemistry, School of Applied Natural Science, Adama Science and Technology University, Adama 251, Ethiopia; Department of Prosthodontics, Saveetha Dental College & Hospital, Saveetha Institute of Medical and Technical Science (SIMATS), Saveetha University, Chennai 600077 Tamil Nadu, India*; orcid.org/0000-0002-2361-086X; Email: anandkps350@gmail.com

Bedasa Abdisa Gonfa − *Department of Applied Chemistry, School of Applied Natural Science, Adama Science and Technology University, Adama 251, Ethiopia*; Email: bedassa.abdissa@astu.edu.et

Taye B. Demissie − *Department of Chemistry, University of Botswana, P.bag UB 00704 Gaborone, Botswana*; orcid.org/0000-0001-8735-4933; Email: demissiet@ub.ac.bw

Authors

Karel G. von Eschwege − *Department of Chemistry, University of the Free State, Bloemfontein 9300, South Africa*; orcid.org/0000-0001-8801-4703

Ernst H. G. Langner − *Department of Chemistry, University of the Free State, Bloemfontein 9300, South Africa*; orcid.org/0000-0002-4667-3396

Elizabeth Coetsee − *Department of Physics, University of the Free State, Bloemfontein ZA9310, South Africa*; orcid.org/0000-0002-9214-4647

Complete contact information is available at: https://pubs.acs.org/10.1021/acsomega.2c08174

Author Contributions

N.A., H.C.A.M., B.A., and T.B.D. designed and performed the experiments, analyzed the data, and wrote the original draft;

https://doi.org/10.1021/acsomega.2c08174
ACS Omega 2023, 8, 13775−13790

N.A., K.G.v.E., E.H.G.L., and E.C. performed the characterization experiments; H.C.A.M., B.A., and T.B.D. supervised the work, and all authors reviewed and edited the manuscript.

Notes

The authors declare no competing financial interest.

■ ACKNOWLEDGMENTS

The authors acknowledge Adama Science and Technology University (ASTU) for supporting this project through the Ministry of Education (MoE) of Ethiopia. In addition, Dr. Lemma TeshomeTufa is acknowledged for hosting the potentiostat facility. The authors extend their acknowledgement to the Department of Construction Technology Management and Food Science and Engineering of Wolkite University, the Department of Applied Chemistry of ASTU, Ethiopia, the Department of Chemistry of the University of Botswana, Botswana, and the University of the Free State, South Africa, for research facilities.

■ REFERENCES

(1) Rahman, M. M.; Sheikh, T. A.; Asiri, A. M.; Alamry, K. A.; Hasnat, M. A. Fabrication of an Ultra-Sensitive Para -Nitrophenol Sensor Based on Facile Zn-Doped Er 2 O 3 Nanocomposites via an Electrochemical Approach. *Anal. Methods* **2020**, *12*, 3470−3483.

(2) Faisal, M.; Alam, M.; Ahmed, J.; Asiri, A. M.; Jalalah, M.; Alruwais, R. S.; Rahman, M. M.; Harraz, F. A. Sensitive Electrochemical Detection of 4-Nitrophenol with PEDOT: PSS Modified Pt NPs-Embedded PPy-CB @ ZnO Nanocomposites. *Biosensors* **2022**, *12*, 990.

(3) Alebachew, N.; Murthy, H. C. A.; Abdissa, B.; Demissie, T. B.; von Eschwege, K. G.; Langner, E. H. G.; Coetsee-Hugo, L. Synthesis and Characterization of CuO@S-Doped g-C 3 N 4 Based Nanocomposites for Binder-Free Sensor Applications. *RSC Adv.* **2022**, *12*, 29959−29974.

(4) Chen, P. Highly Effective Detection of 4-Nitrophenol by Tremella-like Indium Silver Sulfide Modified GCE. *Int. J. Electrochem. Sci.* **2018**, *13*, 6158−6168.

(5) Rahman, M. M.; Marwani, H. M.; Algethami, F. K.; Asiri, A. M.; Hameed, S. A.; Alhogbi, B. Environmental Nanotechnology , Monitoring & Management Ultra-Sensitive p-Nitrophenol Sensing Performances Based on Various Ag 2 O Conjugated Carbon Material Composites. *Environ. Nanotechnol. Monit. Manag.* **2017**, *8*, 73−82.

(6) Singh, S.; Kumar, N.; Kumar, M.; Jyoti; Agarwal, A.; Mizaikoff, B. Electrochemical Sensing and Remediation of 4-Nitrophenol Using Bio-Synthesized Copper Oxide Nanoparticles. *Chem. Eng. J.* **2017**, *313*, 283−292.

(7) Subhan, M. A.; Saha, P. C.; Ahmed, J.; Asiri, A. M.; Al-Mamun, M.; Rahman, M. M. Development of an Ultra-Sensitive Para-Nitrophenol Sensor Using Tri-Metallic Oxide MoO2·Fe3O4·CuO Nanocomposites. *Mater. Adv.* **2020**, *1*, 2831−2839.

(8) Alam, M. M.; Asiri, A. M.; Rahman, M. M. Electrochemical Detection of 2-Nitrophenol Using a Glassy Carbon Electrode Modified with BaO Nanorods. *Chem. − Asian J.* **2021**, *16*, 1475−1485.

(9) Rahman, M. M.; Alam, M. M.; Asiri, A. M. 2-Nitrophenol Sensor-Based Wet-Chemically Prepared Binary Doped Co3O4/Al2O3 Nanosheets by an Electrochemical Approach. *RSC Adv.* **2018**, *8*, 960−970.

(10) Jiang, L.; Yuan, X.; Pan, Y.; Liang, J.; Zeng, G.; Wu, Z.; Wang, H. Doping of Graphitic Carbon Nitride for Photocatalysis: A Reveiw. *Appl. Catal. B Environ.* **2017**, *217*, 388−406.

(11) Zhang, L.; Liu, C.; Wang, Q.; Wang, X.; Wang, S. Electrochemical Sensor Based on an Electrode Modified with Porous Graphitic Carbon Nitride Nanosheets (C3N4) Embedded in Graphene Oxide for Simultaneous Determination of Ascorbic Acid, Dopamine and Uric Acid. *Microchim. Acta* **2020**, *187*, 149.

(12) Chen, G.; Gao, S.-P. Structure and Electronic Structure of S-Doped Graphitic C 3 N 4 Investigated by Density Functional Theory. *Chinese Phys. B* **2012**, *21*, No. 107101.

(13) Ahmad, F. First Principle Calculation of Electronic, Optical Properties and Photocatalytic Potential of CuO Surfaces. *KnE Eng.* **2015**, *2016*, 1−7.

(14) Xu, Y.; Gao, S. Band Gap of C3N4 in the GW Approximation. *Int. J. Hydrogen Energy* **2012**, *37*, 11072−11080.

(15) Dong, F.; Wang, Z.; Sun, Y.; Ho, W.; Zhang, H. Engineering the Nanoarchitecture and Texture of Polymeric Carbon Nitride Semiconductor for Enhanced Visible Light Photocatalytic Activity. *J. Colloid Interface Sci.* **2013**, *401*, 70−79.

(16) Guo, Q.; Zhang, Y.; Qiu, J.; Dong, G. Engineering the Electronic Structure and Optical Properties of G-C 3 N 4 by Non-Metal Ion Doping. *J. Mater. Chem. C* **2016**, *4*, 6839−6847.

(17) Stolbov, S.; Zuluaga, S. Sulfur Doping Effects on the Electronic and Geometric Structures of Graphitic Carbon Nitride Photocatalyst: Insights from First Principles. *J. Phys. Condens. Matter* **2013**, *25*, No. 085507.

(18) Chafi, F. Z.; Salmani, E.; Bahmad, L.; Hassanain, N.; Boubker, F.; Mzerd, A. First Principle Calculations with SIC Correction of Fe-Doped CuO Compound. *Comput. Condens. Matter* **2018**, *16*, No. e00304.

(19) Tian, C.; Zhao, H.; Mei, J.; Yang, S. Cost-Efficient Graphitic Carbon Nitride as an Effective Photocatalyst for Antibiotic Degradation: An Insight into the Effects of Different Precursors and Coexisting Ions, and Photocatalytic Mechanism. *Chem. − Asian J.* **2019**, *14*, 162−169.

(20) Ke, Y.; Guo, H.; Wang, D.; Chen, J.; Weng, W. ZrO 2 /g-C 3 N 4 with Enhanced Photocatalytic Degradation of Methylene Blue under Visible Light Irradiation. *J. Mater. Res.* **2014**, *29*, 2473−2482.

(21) Mohammad, A.; Ehtisham, M.; Hwan, M. Sulfur-Doped-Graphitic -Carbon Nitride (S- g -C 3 N 4) for Low Cost Electrochemical Sensing of Hydrazine. *J. Alloys Compd.* **2020**, *816*, No. 152522.

(22) Tan, L.; Xu, J.; Zhang, X.; Hang, Z.; Jia, Y.; Wang, S. Synthesis of G-C 3 N 4 /CeO 2 Nanocomposites with Improved Catalytic Activity on the Thermal Decomposition of Ammonium Perchlorate. *Appl. Surf. Sci.* **2015**, *356*, 447−453.

(23) He, T.; Wu, Y.; Jiang, C.; Chen, Z.; Wang, Y.; Liu, G.; Xu, Z.; Ning, G.; Chen, X.; Zhao, Y. Novel Magnetic Fe3O4/g-C3N4/MoO3 Nanocomposites with Highly Enhanced Photocatalytic Activities: Visible-Light-Driven Degradation of Tetracycline from Aqueous Environment. *PLoS One* **2020**, *15*, No. e0237389.

(24) Liu, J.; Cheng, B.; Yu, J. A New Understanding of the Photocatalytic Mechanism of the Direct Z-Scheme g-C 3 N 4 /TiO 2 Heterostructure. *Phys. Chem. Chem. Phys.* **2016**, *18*, 31175−31183.

(25) Liu, J. Effect of Phosphorus Doping on Electronic Structure and Photocatalytic Performance of G-C3N4: Insights from Hybrid Density Functional Calculation. *J. Alloys Compd.* **2016**, *672*, 271−276.

(26) Wang, Y.; Tian, Y.; Yan, L.; Su, Z. DFT Study on Sulfur-Doped g-C 3 N 4 Nanosheets as a Photocatalyst for CO 2 Reduction Reaction. *J. Phys. Chem. C* **2018**, *122*, 7712−7719.

(27) Zhang, K.; Zhou, M.; Yu, C.; Yang, K.; Li, X.; Dai, W.; Guan, J.; Shu, Q.; Huang, W. Construction of S-Scheme g-C3N4/ZrO2 Heterostructures for Enhancing Photocatalytic Disposals of Pollutants and Electrocatalytic Hydrogen Evolution. *Dyes Pigm.* **2020**, *180*, No. 108525.

(28) Kavil, J.; Anjana, P. M.; Joshy, D.; Babu, A.; Raj, G.; Periyat, P.; Rakhi, R. B. G-C 3 N 4 /CuO and g-C 3 N 4 /Co 3 O 4 Nanohybrid Structures as Efficient Electrode Materials in Symmetric Supercapacitors. *RSC Adv.* **2019**, *9*, 38430−38437.

(29) Miyamoto, Y.; Cohen, M. L.; Louie, S. G. Theoretical Investigation of Graphitic Carbon Nitride and Possible Tubule Forms. *Solid State Commun.* **1997**, *102*, 605−608.

(30) Manoharan, D.; Loganathan, A.; Kurapati, V.; Nesamony, V. J. Ultrasonics Sonochemistry Unique Sharp Photoluminescence of Size-Controlled Sonochemically Synthesized Zirconia Nanoparticles. *Ultrason. − Sonochem.* **2015**, *23*, 174−184.

https://doi.org/10.1021/acsomega.2c08174
ACS Omega 2023, 8, 13775−13790

(31) Wang, Y.; Zhang, Y.; Lu, H.; Chen, Y.; Liu, Z.; Su, S.; Xue, Y.; Yao, J.; Zeng, H. Novel N-Doped ZrO 2 with Enhanced Visible-Light Photocatalytic Activity for Hydrogen Production and Degradation of Organic Dyes. *RSC Adv.* **2018**, *8*, 6752−6758.
(32) Horti, N. C.; Kamatagi, M. D.; Nataraj, S. K.; Wari, M. N.; Inamdar, S. R. Structural and Optical Properties of Zirconium Oxide (ZrO 2) Nanoparticles: Effect of Calcination Temperature. *Nano Express* **2020**, *1*, No. 010022.
(33) Bi, X.; Yu, S.; Liu, E.; Yin, X.; Zhao, Y.; Xiong, W. Nano-Zirconia Supported by Graphitic Carbon Nitride for Enhanced Visible Light Photocatalytic Activity. *RSC Adv.* **2019**, *10*, 524−532.
(34) Zarei, M. Ultrasonic-Assisted Preparation of ZrO2/g-C3N4 Nanocomposites with High Visible-Light Photocatalytic Activity for Degradation of 4-Chlorophenol in Water. *Water-Energy Nexus* **2020**, *3*, 135−142.
(35) Guo, H.; Shu, Z.; Chen, D.; Tan, Y.; Zhou, J.; Meng, F.; Li, T. One-Step Synthesis of S-Doped g-C3N4 Nanosheets for Improved Visible-Light Photocatalytic Hydrogen Evolution. *Chem. Phys.* **2020**, *533*, No. 110714.
(36) Harish, V.; Ansari, M.; Tewari, D.; Gaur, M.; Yadav, A. B. Nanoparticle and Nanostructure Synthesis and Controlled Growth Methods. *Nanomaterials* **2022**, *12*, 3226.
(37) Khan, S. B.; Rahman, M. M.; Akhtar, K.; Asiri, A. M.; Rub, M. A. Nitrophenol Chemi-Sensor and Active Solar Photocatalyst Based on Spinel Hetaerolite Nanoparticles. *PLoS One* **2014**, *9*, No. e85290.
(38) Frisch, M. J.; Trucks, G. W.; Schlegel, H. B.; Scuseria, G. E.; Robb, M. A.; Cheeseman, J. R.; Scalmani, G.; Barone, V.; Petersson, G. A.; Nakatsuji, H.; Li, X.; Caricato, M.; Marenich, A. V.; Bloino, J.; Janesko, B. G.; Gomperts, R.; Mennucci, B.; Hratchian, H. P.; Ortiz, J. V.; Izmaylov, A. F.; Sonnenberg, J. L.; Williams-Young, D.; Ding, F.; Lipparini, F.; Egidi, F.; Goings, J.; Peng, B.; Petrone, A.; Henderson, T.; Ranasinghe, D.; Zakrzewski, V. G.; Gao, J.; Rega, N.; Zheng, G.; Liang, W.; Hada, M.; Ehara, M.; Toyota, K.; Fukuda, R.; Hasegawa, J.; Ishida, M.; Nakajima, T.; Honda, Y.; Kitao, O.; Nakai, H.; Vreven, T.; Throssell, K.; Montgomery, Jr., J. A.; Peralta, J. E.; Ogliaro, F.; Bearpark, M. J.; Heyd, J. J.; Brothers, E. N.; Kudin, K. N.; Staroverov, V. N.; Keith, T. A.; Kobayashi, R.; Normand, J.; Raghavachari, K.; Rendell, A. P.; Burant, J. C.; Iyengar, S. S.; Tomasi, J.; Cossi, M.; Millam, J. M.; Klene, M.; Adamo, C.; Cammi, R.; Ochterski, J. W.; Martin, R. L.; Morokuma, K.; Farkas, O.; Foresman, J. B.; Fox, D. J. *Gaussian 09 Revision C-01*; Gaussian, Inc.: Wallingford, CT, 2009.
(39) Becke, A. D. Density - Functional Thermochemistry. III . The Role of Exact Exchange. *J. Chem. Phys.* **2005**, *98*, 5648.
(40) Lee, C.; Yang, W.; Parr, R. G. Development of the Colle-Salvetti Correlation-Energy Formula into a Functional of the Electron Density. *Phys. Rev. B* **1988**, *37*, 785−789.
(41) Stephens, P. J.; Devlin, F. J.; Chabalowski, C. F.; Frisch, M. J. Ab Initio Calculation of Vibrational Absorption and Circular Dichroism Spectra Using Density Functional Force Fields. *J. Phys. Chem.* **1994**, *98*, 11623−11627.
(42) Liu, J.; Zhang, T.; Wang, Z.; Dawson, G.; Chen, W. Simple Pyrolysis of Urea into Graphitic Carbon Nitride with Recyclable Adsorption and Photocatalytic Activity. *J. Mater. Chem.* **2011**, *21*, 14398.
(43) López, R.; Gómez, R. Band-Gap Energy Estimation from Diffuse Reflectance Measurements on Sol−Gel and Commercial TiO2: A Comparative Study. *J. Sol-Gel Sci. Technol.* **2012**, *61*, 1−7.
(44) Zou, J.; Yu, Y.; Yan, W.; Meng, J.; Zhang, S.; Wang, J. A Facile Route to Synthesize Boron-Doped g-C3N4 Nanosheets with Enhanced Visible-Light Photocatalytic Activity. *J. Mater. Sci.* **2019**, *54*, 6867−6881.
(45) Li, Y.; Ho, W.; Lv, K.; Zhu, B.; Lee, S. C. Carbon Vacancy-Induced Enhancement of the Visible Light-Driven Photocatalytic Oxidation of NO over g-C 3 N 4 Nanosheets. *Appl. Surf. Sci.* **2018**, *430*, 380−389.
(46) Ke, Y.; Guo, H.; Wang, D.; Chen, J.; Weng, W. ZrO2/g-C3N4 with Enhanced Photocatalytic Degradation of Methylene Blue under Visible Light Irradiation. *J. Mater. Res.* **2014**, *29*, 2473−2482.
(47) Singh, P. P.; Srivastava, V. Recent Advances in Visible-Light Graphitic Carbon Nitride (g-C 3 N 4) Photocatalysts for Chemical Transformations. *RSC Adv.* **2022**, *12*, 18245−18265.
(48) Lackner, P.; Zou, Z.; Mayr, S.; Diebold, U.; Schmid, M. Using Photoelectron Spectroscopy to Observe Oxygen Spillover to Zirconia. *Phys. Chem. Chem. Phys.* **2019**, *21*, 17613−17620.
(49) Lui, G.; Liao, J.; Duan, A.; Zhang, Z.; Fowler, M.; Yu, A. Graphene-Wrapped Hierarchical TiO2 Nanoflower Composites with Enhanced Photocatalytic Performance. *J. Mater. Chem. A* **2013**, *1*, 12255.
(50) Nehru, R.; Gopi, P. K.; Chen, S. Enhanced sensing of hazardous 4-nitrophenol by a graphene oxide−TiO2 composite: environmental pollutant monitoring applications. *New J. Chem.* **2020**, *44*, 4590−4603.
(51) Mohammad, A.; Khan, M. E.; Cho, M. H. Sulfur-Doped-Graphitic-Carbon Nitride (S-g-C3N4) for Low Cost Electrochemical Sensing of Hydrazine. *J. Alloys Compd.* **2020**, *816*, No. 152522.
(52) Wang, R.; Wang, Y.; Mao, S.; Hao, X.; Duan, X.; Wen, Y. Different Morphology MoS2 Over the G-C3N4 as a Boosted Photo-Catalyst for Pollutant Removal Under Visible-Light. *J. Inorg. Organomet. Polym. Mater.* **2021**, *31*, 32−42.
(53) Yang, X.; Qian, F.; Zou, G.; Li, M.; Lu, J.; Li, Y.; Bao, M. Facile Fabrication of Acidified G-C3N4/g-C3N4 Hybrids with Enhanced Photocatalysis Performance under Visible Light Irradiation. *Appl. Catal. B Environ.* **2016**, *193*, 22−35.
(54) Dhanasekaran, T.; Manigandan, R.; Padmanaban, A.; Suresh, R.; Giribabu, K.; Narayanan, V. Fabrication of Ag@Co-Al Layered Double Hydroxides Reinforced Poly(o-Phenylenediamine) Nano-hybrid for Efficient Electrochemical Detection of 4-Nitrophenol, 2,4-Dinitrophenol and Uric Acid at Nano Molar Level. *Sci. Rep.* **2019**, *9*, 13250.
(55) Cheng, Y. A Sensor for Detection of 4-Nitrophenol Based on a Glassy Carbon Electrode Modified with a Reduced Graphene Oxide/Fe3O4 Nanoparticle Composite. *Int. J. Electrochem. Sci.* **2017**, *12*, 7754−7764.
(56) Chu, L.; Han, L.; Zhang, X. Electrochemical Simultaneous Determination of Nitrophenol Isomers at Nano-Gold Modified Glassy Carbon Electrode. *J. Appl. Electrochem.* **2011**, *41*, 687−694.
(57) Bhujel, R.; Rai, S.; Baruah, K.; Deka, U.; Biswas, J.; Swain, B. P. Capacitive and Sensing Responses of Biomass Derived Silver Decorated Graphene. *Sci. Rep.* **2019**, *9*, 19725.

https://doi.org/10.1021/acsomega.2c08174
ACS Omega 2023, 8, 13775−13790